İSTANBUL TECHNICAL UNIVERSITY ★ INSTITUTE OF SCIENCE AND TECHNOLOGY

MEMS ACCELEROMETER DESIGN

M.Sc. Thesis by
Özgür ERDENER, B.Sc.

Department : **Electronics and Communication Engineering**
Programme: **Electronics Engineering**

MAY 2005

İSTANBUL TECHNICAL UNIVERSITY ★ INSTITUTE OF SCIENCE AND TECHNOLOGY

MEMS ACCELEROMETER DESIGN

M.Sc. Thesis by
Özgür ERDENER, B.Sc.
(504021214)

Date of submission : 9 May 2005

Date of defence examination: 2 June 2005

Supervisor (Chairman): Prof. Dr. Ali TOKER

Co-Supervisor: Assist. Prof.Dr. Levent TRABZON

Members of the Examining Committee: Assoc. Prof.Dr. Ali ZEKİ

Assoc. Prof.Dr. Coşkun SÖNMEZ

Assist. Prof.Dr. Nil TARIM

MAY 2005

ACKNOWLEDGMENT

I would like to thank my supervisors Prof. Dr. Ali TOKER and Assoc. Prof. Dr. Levent TRABZON for introducing me to MEMS and giving me the opportunity of implementing my thesis, for their endless support, and special thanks for teaching me to think scientific.

Also, I would like to thank Assoc. Prof. Dr. Ali ZEKI for his technical support.

I am very grateful to Christopher GRINDE from Vestfold University College, Norway because of his kind support about ANSYS.

Finally, I would like to dedicate my thesis to my lovely family, who supported me at every stage of all my life.

May 2005 Özgür ERDENER

CONTENTS

TABLE LIST

Page No

FIGURE LIST

MEMS İVME ÖLÇER TASARIMI

ÖZET

Mikroelektromekanik Sistemler (MEMS) ile ilgili çalışmalar 1960'ların sonlarında ,tümleşik devrelerin üretiminde kullanılan fabrikasyon yöntemlerinin küçük değişiklikler yapılarak, minyatür mekanik elemanların üretiminde de kullanılabileceğinin düşünülmesi ile başlamıştır. Bu mekanik sitemler içerisinde günümüzde en ticari olmuşlarından biri ivme ölçerlerdir ve bu konuyla ilgili bilimsel çalışmalar halen yoğun bir şekilde sürdürülmektedir. Bu çalışmada, analog kapasitif MEMS ivme ölçer sisteminin teori, tasarım süreci ve analizi incelenmiş ve yüzey mikro makine tekniği olan MUMPS prosesi kullanılarak geniş ölçme dinamiğine sahip MEMS ivme ölçer sistemi gerçeklenmiştir. Mekanik sistemin optimizasyonu için Bölüm 2'de elde edilen analitik modeller kullanılarak C++ programla dilinde MABEMS isimli görsel tabanlı bir program yazılmıştır. Mekanik sisteminlerin sonlu eleman analizlerinde ticari bir yazılım olan ANSYS kullanılmıştır. Davranışsal seviyedeki simulasyonlar içinse sistemin MATLAB Simulink modeli oluşturulmuştur. Elektronik algılama kısmında, parazitik kapasitelerin etkisini azalttığı için yük kuvvetlendiricisi yapısı kullanılmıştır. İvme ölçerin Bölüm 3'te elde edilen matematik modeli, analog davranışsal modelleme kütüphanesi (ABM) kullanılarak PSPICE içerisinde gerçeklenmiş ve bu da elektronik algılama devresi ile mekanik elemanın aynı ortamda simulasyonuna olanak vermiştir. Geleneksel yöntemlerde, MEMS ivme ölçerler, ölçme dinamiği, band genişliği ve lineerlik gibi performans ölçütlerinin iyileştirilmesi için geri beslemeli çevrimde çalıştırılır. Bu çalışmada, bu yönteme alternatif olarak ölçme hassasiyeti düşük olan bir sistemin, hassasiyeti daha yüksek olanın dinamik ofsetini (sıfırını) oluşturması prensibine dayanan ve "Kuvvet İleri Beslemesi" diye isimlendirdiğimiz yöntem önerilmiş ve kavramsal olarak tanımlanmıştır. Bu amaçla biri daha hassas fakat belli bir yer değiştirme değerinden sonra lineerliği bozulan, diğeri de daha az hassas fakat her zaman lineer çıkış veren iki farklı mekanik sistem tasarlamıştır. Tasarımlara ilişkin bütün sonuçlar Bölüm 3'te verilmiştir.

MEMS ACCELEROMETER DESIGN

SUMMARY

Works about the Microelectromechanical Systems (MEMS) has begun in the late 1960’s, when researchers began to think about that the fabrication technology, which is used for manufacturing of integrated electronic circuits, with only slight modifications, could also be used for fabrication of the mechanical components in miniature scale. Today, one of the most commercialized system in this area is accelerometers and also scientific work about this topic is still carried on. In this work, the theory, design process, and analysis of analog capacitive MEMS accelerometer system is examined and a high dynamic range MEMS accelerometer system is implemented by using MUMPS surface micromachining process. For the optimization of the mechanical system, by using the analytical models obtained in Section 2, a visual software, named MABEMS, is implemented in C++ programming language. Finite element analysis of the mechanical systems are made by using a commercially available simulation package ANSYS. MATLAB Simulink model of the system is realized for the behavioral level simulations. The charge amplifier topology is used in electronic sensing interface since this configuration eliminates the effect of the parastic capacitances. Mathematical model of the accelerometer, obtained in Section 3, is implemented in PSPICE by using the Analog Behavioral Modelling (ABM) library so, this allowed the simulation of the mechanical device and electronic interface in the same environment. In conventional methods, accelerometers are operated in closed loop by applying feedback signals to increase the performance parameters like dynamic range, bandwidth, and linearity. In this work, a new method is offered and described conceptually as an alternative to the conventional closed loop systems and this method is named as Force Feed forward Mechanism. In this method, less sensitive system, forms the dynamic offset of the more sensitive device. For this reason, two different mechanical devices are designed such that one of them has high sensitivity but nonlinear output above a certain displacement and the other one has low sensitivity but linear even for large displacements. All the results about the designed systems are given in Section 3.

1 INTRODUCTION

1.1 MEMS Overview

In the late 1960's, researchers began to think about that the fabrication technology, which is used for manufacturing of integrated electronic circuits, with only slight modifications, could also be used for fabrication of the mechanical components in miniature scale. Consequence of these researches, a new technology that allows the manufacturing of Micro Electro Mechanical Systems (MEMS) was born. As a general definition, MEMS are the units that contain mechanical components and its related electronic interface with the size ranging from nanometers to hundreds of microns. In Europe, the term "Microsystems" is used instead of MEMS as a more general and more inclusive name. There are mainly three micromachining techniques; bulk micromachining, surface micromachining, and high aspect ratio techniques. Bulk micromachining, processes where the mechanical structures are realized by etching a bulk material, was the first implemented micromachining technique for manufacturing of pressure sensors in early 1960's. In this technique, the mostly used bulk material is Single-Crystalline-Silicon (SCS). Thickness of the bulk micromachined structures range from submicron to full wafer thickness (~500 μm), and lateral dimensions can be as large as a few millimeters. Some of the bulk micromachined devices utilize the anodic bonding of glass and silicon wafers to create the hermetically sealed cavities or fusion bonding of silicon wafers to obtain complex geometry and high sensitivity devices. Surface micromachining, processes where the thin films of different materials are deposited on a bulk silicon and then a sacrificial thin film is selectively etched to release the movable structures, was invented by R. Howe and R. Muller in 1982 and has become the mostly used technique for the fabrication of today's commercially available sensors and actuators. This technology allows to monolithicaly integrate the mechanical and electronic components on the same wafer. In the late 1980's, new micromachining techniques, which use materials other than used in integrated circuit (IC) processing, has emerged especially for manufacturing of high aspect ratio structures but much of them are not compatible with the processes that are currently used for IC manufacturing. For this reason, these techniques are not yet commercialized.

Small size, batch fabrication, low cost and low power consumption are the key advantages of MEMS technology. Also, performance parameters like reliability, accuracy, flexibility, and sensitivity of micromachined systems are often better when compared with their conventional counterparts. For these reasons, today, micromachined systems have found wide application areas as summarized in Table 1.1. For the Integration of the mechanical device and associated electronic interface, mainly there are three methods; Monolithic Integration method in which the mechanical structures and electronic interface are processed on the same die, Flip Chip method in which the mechanical device and electronics are manufactured separately and combined in the same package by using electroplated solders to create bumps for face to face attachment of separate dies, and Hybrid Chip method in which the mechanics and electronics are manufactured separately and combined in the same package by wire bonding. Today's most commercialized microsystems use the standart packages, which are utilized for packaging of integrated electronic circuits. Packaging effects are crucial for overall performance of microsystems, especially for precision systems, but this subject is not in the scope of this thesis and detailed knowledge can be found in [1,2,3,4,5].

Table 1.1: Application of MEMS technology

Application Area	**Products**
Automotive sensors	Accelerometers, force/torque sensors, environmental monitoring, pressure sensors,
Bio MEMS	Micro total analysis system (µTAS), clinical diagnostics, drug delivery systems, DNA sequencing chips, blood pressure sensing
Chemistry	Lab-on-a-chip (microreactors)
Optics	Digital micromirror devices, Optical interconnects (switching and routing)
Data storage	Precision servo, new data storage techniques, shock sensors for HDD
RF for communication	MEMS Switches, filters, tunable banks
Power generation	MEMS turbine engines, fuel cells, MEMS power generators
Aerospace	Aircraft, micro-satallites, space exploration
Microfluidics	Flowmeters, Mass Flow Sensors, Fluidic Amplifiers, Ink Jet Heads
Recent researches	Harsh environment MEMS, MEMS/nano hybrid system (NEMS**)**

1.2 Silicon Material in MEMS Technology

There are many different materials used in MEMS technology [1,2,4,6], but most of today's micromachining technology is based on silicon since its properties are widely studied and documented and, the tools and the equipments used for fabrication of ICs are designed to meet the properties of silicon. The properties of silicon allow it to be a suitable material platform on which electronic, thermal, mechanical, optical, and fluid flow functions can be realized. Silicon element exists in crystalline, polycrystalline, or amorphous form.

Single-crystal-silicon (SCS) can be used as conductive or piezoresistive material or etch stop layer in wet etching by doping with the appropriate atoms. But it is mostly utilized as structural material in displacement sensors like pressure sensors and accelerometers. For a structural material the most important mechanical parameter is Young's Modulus, which is the measure of elasticity of material. SCS has mechanical anisotropy, which makes its Young's Modulus crystal orientation dependent. For this reason, to obtain the variation of Young's Modulus value with respect to crystal orientation, stiffness tensor referred to <100> orientation can be defined as:

$$\begin{bmatrix} \sigma_x \\ \sigma_y \\ \sigma_z \\ \tau_{yz} \\ \tau_{zx} \\ \tau_{xy} \end{bmatrix} = C \times \varepsilon = \begin{bmatrix} 165.6 & 63.98 & 63.98 & 0 & 0 & 0 \\ 63.98 & 165.6 & 63.98 & 0 & 0 & 0 \\ 63.98 & 63.98 & 165.6 & 0 & 0 & 0 \\ 0 & 0 & 0 & 79.51 & 0 & 0 \\ 0 & 0 & 0 & 0 & 79.51 & 0 \\ 0 & 0 & 0 & 0 & 0 & 79.51 \end{bmatrix} \begin{bmatrix} \varepsilon_x \\ \varepsilon_y \\ \varepsilon_z \\ \gamma_{yz} \\ \gamma_{zx} \\ \gamma_{xy} \end{bmatrix} \tag{1.1}$$

Brantley's formula [2] is utilized for obtaining the crystal orientation dependent Young's Modulus.

$$\frac{1}{E} = \left[S_{11} - 2 \times (S_{11} - S_{12} - \frac{1}{2} \times S_{44}) \times (l_1^2 \times l_2^2 + l_2^2 \times l_3^2 + l_1^2 \times l_3^2) \right] \tag{1.2}$$

S_{ij} is the jth element in ith row in the compliance matrix, which is the inverse of stiffness matrix (***C***). l_1, l_2, l_3 are directions cosines with respect to cubic axis. By using equation (1.2) a program is written in MATLAB to obtain Young's Modulus for SCS in different directions. Graphical output of program is shown in Figure 1.1 and Listing of program can be found in Appendix A.

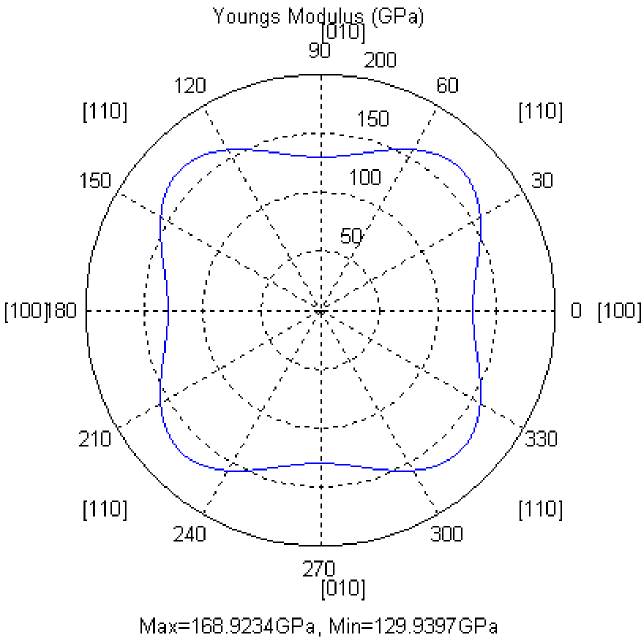

Figure 1.1: Young's Modulus vs. orientation in polar coordinates

Polycrystalline silicon thin films are grown instead of SCS since it is diffucult to grow thin films of SCS. Today, most of the commercialy available mechanical sensors utilize polysilicon thin films as the structural material. It can also be used as conductive or piezoresistive material by doping with appropriate atoms. Polycrystalline silicon thin films are usually deposited with typical thickness below 5 μm. It is deposited by using the process, called Low Pressure Chemical Vapor Deposition (LPCVD) with pyrolization of Silane (SiH_4). It can be doped in situ with diborane (B) or phosphine (P) atoms or after deposition via BSG/PSG diffusion. Doping level dictates electrical conductivity. Electromechanical properties of polysilicon strongly depend on grain structure, which varies with growth temperature. Between 600 ^{0}C and 625 ^{0}C <110> oriented fine grains are dominant in polysilicon structure. In this case, it has rougher surface and residual stress is compressive. Between 625 ^{0}C and 650 ^{0}C columnar grains are dominant. And, between 650 ^{0}C and 700 ^{0}C <100> oriented large grains, which cause smooth surface, tensile residual stress is dominant. Relatively high levels of intrinsic stress occur during the deposition of polysilicon, for this reason it requires annealing at elevated temperatures (>900 ^{0}C) after deposition.

Young's modulus, Poisson's ratio and the tensile strength of the polysilicon thin films are required for intelligent structural mechanical device design. Two of these parameters are related to the stiffness of material and the last one is related to the failure of material. In this thesis, since the Multi-User MEMS Process (MUMPs), in which the structural layer is polysilicon thin film, is used to design the mechanical parts of the accelerometer system, it is imperative to employ the exact values of these three parameters. The authors in [7] have developed techniques and procedures that permit the measurement of these parameters of 3.5 micrometers thick polysilicon thin films. They made the measurements on the specimens from PolyMUMPs runs.

As it will be explained in Section 2.2, for modeling the dynamic behavior of accelerometer system, three parameters should be well determined. These parameters are mass, stiffness coefficient, and damping coefficient. All of these parameters depend on firstly geometrical dimensions and topology. In addition, mass and stiffness coefficient depends on material properties of structural layer and damping factor depends on environment in which the mechanical device operates. In this work, mechanical device is designed by using MUMPs process and the operation environment of device is air. Table 1.5 shows the parameter values that are used along this thesis for the modeling of mechanical parts of the accelerometer system.

Table 1.2: Mechanical parameters, used along this thesis

Parameter	Value
Young's Modulus (GPa)	169 [7]
Poisson's Ratio	0.22 [7]
Tensile Strength (GPa)	1.20 [7]
Density (kg/m^3)	2330
Viscosity of Air (kg/m.s) [18^0C, 760 Torr]	$1.827\ 10^{-5}$ [1]

1.3 MEMS Design Process

In the MEMS technology, design of the full system is extremely difficult job because of the interdisciplinary nature of the system and the large number of system interactions. Depending to the application, design of the full system can necessitate collaboration of the many people from different disciplines like biology, mechanics, electronics, chemistry, physics etc. As well established MEMS process technologies have emerged, researchers began to be interested with the design of systems that contain too many mixed domain components. Over the past ten years, a couple of commercially available CAD software that allows the top-down design of MEMS has made the design process less time consuming work. Examples of these commercial MEMS Design Suites are MEMSPro from MemsCap, CoventorWare from Coventor, IntelliSuite from IntelliSuite Technologies, Inc. etc.

A microsystem design process includes all the activities required for obtaining the mask layout, which is used for manufacturing in a foundry, from the system specifications [8]. And also, the specific steps may require the utilization of CAD software tools. Design process flow chart for the accelerometer system that is implemented in this thesis is shown in Figure 1.2. The definitions written in italics are not the steps that are applied in this work but depending to the design, they can be inevitable to follow.

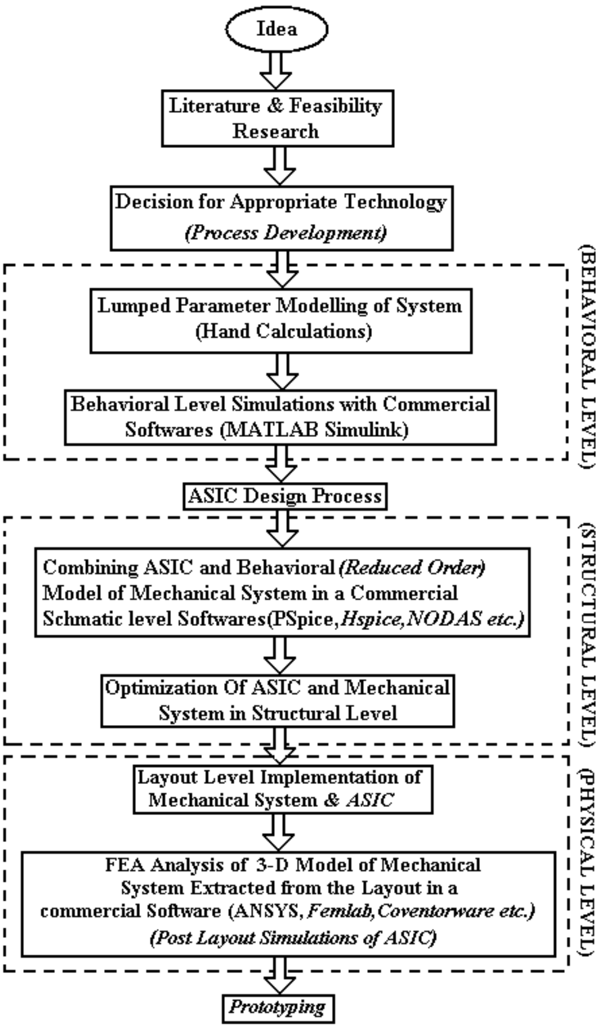

Figure 1.2: Design process flow, followed for the design of accelerometer system in this thesis

1.4 MEMS Accelerometer Overview

An accelerometer converts the acceleration, caused by a motion or gravity, to an electrical signal. Since the accelerometers can measure the earth's gravity they can be used to detect a change in tilt so, these kinds are used for applications such as car alarms, game joysticks and patient activity monitors. And also, the velocity or distance or force can be measured since the acceleration integrated over time equals to the velocity and the velocity integrated over time results in distance. This property is used for death reckoning in Global Positining Systems (GPS). Additionally, they can also be used to measure vibrations, for example, from rotating equipment or earthquakes.

The first micromachined accelerometer is implemented in 1979 at Stanford University, but the commercialization of these devices took nearly 20 years. Today, there are many commercially available accelerometers from many different manufacturers. Depending to the application area, these accelerometers have different specifications. Analog Device's surface micromachined accelerometers (ADXL Family) is a good example of commercially available MEMS accelerometers. Anolog Device uses monolithic integration technology (iMEMS), which allows to realize the mechanical device and electronic circuitry on the same chip for obtain better sensitivity and performance [9]. Motorola's MMA family of surface micromachined accelerometers uses the two chip technology for combining the mechanical device and electronic interface and the sensing element has been sealed hermetically at the wafer level using a bulk micromachined "cap" wafer. [10]. Endevco's bulk micromachined, out-of-plane, SCS accelerometers uses two chip solution that are integrated in one package. All of these commercial accelerometers uses capacitive sensing mechanisms. Experimental evaluation and comparative analysis of these commercial MEMS accelerometers are well described in [11]. Also, there are many other MEMS accelerometer manufacturing companies like ST Microelectronics [12], Silicon Designs etc.

In addition to the commercially available MEMS accelerometers, because of the wide application areas and need for better resolution and sensitivity there are still many implemented and continuing researches for improving their performance. Performance parameters and design considerations of capacitive MEMS accelerometers (for both electronic interface and mechanical device) are well studied in [13]. A high sensitive, bulk micromachined (by using Deep Reactive Ion Etching-DRIE), Silicon-On-Glass capacitive micro accelerometer capable of micro-g performance has been reported in [14]. A fully-integrated biaxial (with single proofmass to detect in-plane accelerations at x and y-axis) linear accelerometer realized in a standard 0.5μm CMOS technology for high sensitivity applications has been reported in [15] . A bulk micromachined CMOS integrated three-axis accelerometer (electronic interface is on the proofmass) with single proofmass has been reported in [16]. In the work realized in [16], for the detection of acceleration, p type MOSFETs are used as stress sensitive elements to transform the deflection of the beam structures caused by input acceleration into electrical signal. [17] has reported a lateral CMOS-MEMS accelerometer with a measured noise floor of 1mg/$\sqrt{Hz}$ and a dynamic range larger than 13 g. Three-axis (with three different proofmass) surface micromachined monolithically integrated accelerometer with offset-trim electronics has been presented in [18]. A three-axis force balanced surface micromachined monolithic accelerometer using a single proofmass has been proposed in [19]. It presents a new method for wideband force balancing of a proofmass in multiple axes simultaneously. A SCS accelerometer, which has been fabricated using Silicon Fusion Bonding (SFB) and Deep Reactive Ion Etching (DRIE) with mg resolution has been reported in [20]. A vacuum packaged surface micromachined resonant accelerometer has been reported in [21]. A thermal accelerometer based on heat transfer mechanism has been reported in [22]. In this design polysilicon-aluminium thermopiles are used to determine the temperature difference between the seismic mass heatsink and heatsource.

1.5 MUMPS Process Description

In this work, the mechanical parts of the MEMS accelerometer system is designed by using the Polysilicon Multi-User MEMS Process, or PolyMUMPs® which is a commercial programme that can be utilized by universities or industry for cost-effective MEMS fabrication. Access to this technology is provided by MemsCap Inc. PolyMUMPs is a three-layer[1] polysilicon surface micromachining process and designed for all MEMS designers as a general-purpose micromachining technology.

[1] Generally it is named as 2.5 layer process since POLY0 layer could only be used as base contact (electrode) or conductor not as a structural material like POLY1 and POLY2.

Therefore, this process is explained in detail, in this section, as it is described in design handbook [23].

Process begins by heavily doping the surface of an n-type (100) wafer with phosphorus. A low stress silicon nitride layer with the thickness of 600 nm is deposited to provide electrical isolation between the substrate and above layers and this is followed by the deposition of 500 nm thick polysilicon layer (POLY0). Then UVsensitive photoresist is spread over the polysilicon layer (Figure 1.3a). The photoresist is patterned with the POLY0 mask and developed. Unwanted polysilicon is then removed by utilizing the Reactive Ion Etching (RIE) technique and photoresist is stripped chemically from the surface (Figure 1.3b). In a LPCVD furnace, a layer of phospho silicate glass (PSG) with the thickness of 2.0 μm is deposited and then 750 nm deep dimples are rective ion etched into this oxide layer that serves as first sacrificial layer (Figure 1.3c). A photoresist is spread over again and ANCHOR1 mask is utilized to lithographically pattern the photoresist. The unwanted oxide is removed by RIE and photoreist is stripped (Figure 1.3d). In a LPCVD furnace, a layer of undoped polysilicon with the thickness of 2.0 μm is deposited and this is followed by the deposition of 200 nm thick PSG. For the doping of undoped polysilicon and for reducing its residual stress, an annealing process at 1050°C is carried out for one hour (Figure 1.3e). A photoresist is spread over again and POLY1 mask is utilized to lithographically pattern the photoresist. Firstly, PSG layer is etched to make a hard mask and then Poly1 layer is etched. After the etch process, PSG hard mask and resist are removed (Figure 1.4a). A PSG layer that serve as second sacrificial oxide layer with the thickness of 0.75 μm is deposited (Figure 1.4b). A photoresist is spread over again and POLY1_POLY2_VIA mask is utilized to lithographically pattern the photoresist. The unwanted second oxide layer is removed by RIE until etch process stops at Poly1 layer and photoreist is stripped (Figure 1.4c). A photoresist is spread over again and ANCHOR2 mask is utilized to lithographically pattern the photoresist. The unwanted second oxide layer is removed by RIE until etch process stops at Poly 0 or silicon nitride layer and photoreist is stripped (Figure 1.4d). A layer of undoped polysilicon with the thickness of 1.5 μm is deposited again and this is followed by the deposition of 200 nm thick hard-mask PSG. To dope the undoped polysilicon and to reduce its residual stress, an annealing process at 1050°C is again carried out for one hour (Figure 1.4e). A photoresist is spread over again and POLY2 mask is utilized to lithographically pattern the photoresist. PSG layer and Poly1 layer are etched by RIE. After the etch process is finished, PSG hard mask and photoresist are removed (Figure 1.4f). A photoresist is spread over and METAL mask is utilized to lithographically pattern the photoresist. A layer of gold with a thin adhesion layer is deposited by utilizing lift-off patterning technique, so the unwanted metal stays at the top of the photoresist and both of them are lifted-off (Figure 1.4g). In the end, by immersing the fabricated chips in a HF solution (ratio of HF in solution is 49%) all the structural parts are released (Figure 1.4h).

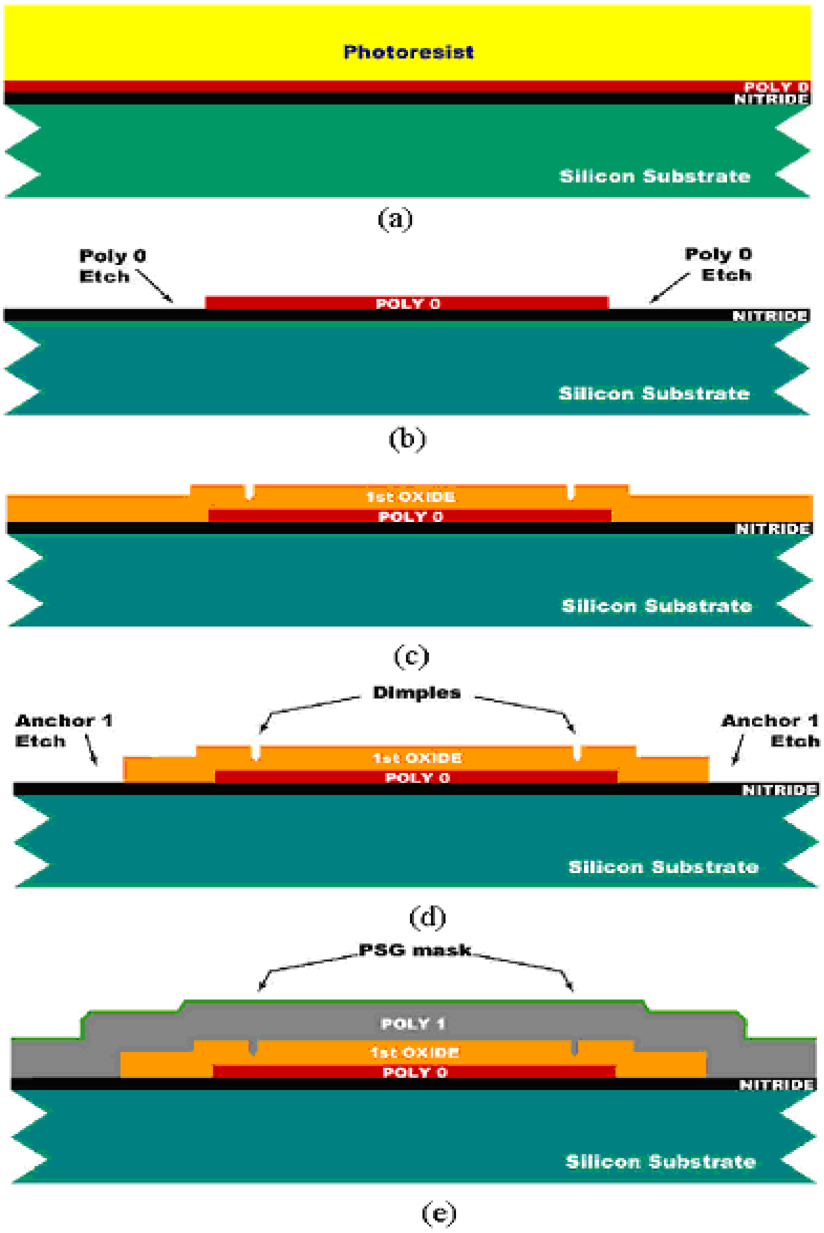

Figure 1.3: Illustration of PolyMUMPs process steps I [23]

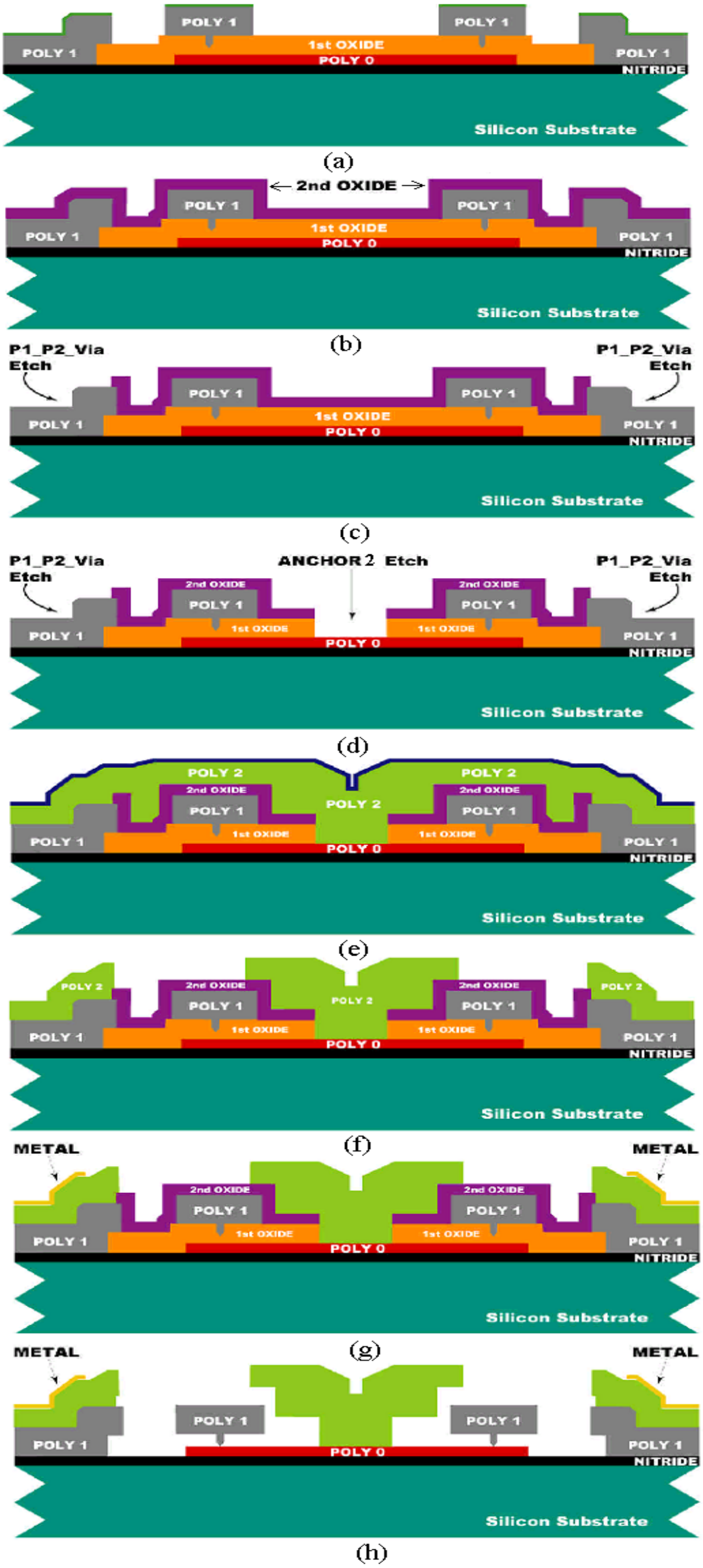

Figure 1.4: Illustration of PolyMUMPs process steps II [23]

2 LUMPED PARAMETER MODELING OF MEMS ACCELEROMETER

2.1 Introduction

Analytical expressions should be obtained to determine the performance parameters of the accelerometer system. In this section, the lumped parameter models, which describe the behaviour of the overall system, are defined and analytical expressions of these parameters are derived as a function of the physical design variables. Obtained models, along this section, include the damping effects, electrostatic effects, effective spring constant, sensitivity of the device, and the capacitive sensing interface.

2.2 Dynamic Model

At behavioral level, accelerometers are modeled as spring-mass-damper systems as shown in Figure 2.1. From the free body diagram in Figure 2.1 differential equation for the displacement of the mass as a function of external acceleration is:

$$m\frac{d^2x(t)}{dt^2}+b\frac{d^2x(t)}{dt^2}+k.x(t)=m\frac{d^2y(t)}{dt^2}=m.a_{ext}(t) \qquad (2.1)$$

where k is the spring stiffness, b is the damping coefficient, m is the effective mass and a_{ext} is the external acceleration that effects the system.

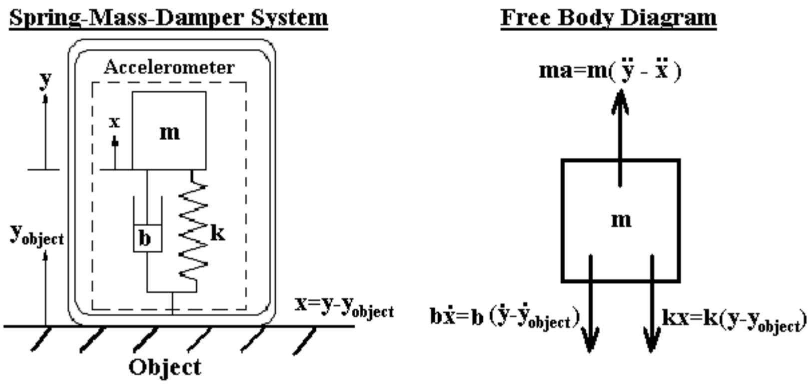

Figure 2.1: Spring-mass-damper system and related free body diagram

If Laplace transform is applied to the second-order system given by equation (2.1), the frequency response of the system is found as:

$$\frac{X(s)}{A_{ext}(s)} = \frac{1}{s^2 + \frac{b}{m}s + \frac{k}{m}} = \frac{1}{s^2 + \frac{\omega_r}{Q}s + \omega_r^2} \tag{2.2}$$

In equation (2.2), $\omega_r = \sqrt{k/m}$ is the resonant frequency and $Q = \omega_r m/b = \sqrt{km}/b$ is the quality factor. If the quality factor of the system is less than 0.5 it is named as over damped system, if quality factor is equal to 0.5 the system is critically damped, and for Q>0.5 the system is under damped. Under damped systems are preferred because of the low mechanical noise (Section 2.6) and quick response time. Over damped systems have the disadvantage of high mechanical noise and low bandwidth. For these reasons, quality factor has an important effect on the performance of accelerometer. As it is clear from equation (2.2), at frequencies much lower than the resonant $(\omega_r << \omega)$, the mechanical sensitivity can be defined as:

$$\frac{x(t)}{a(t)} \approx \frac{1}{\omega_r^2} = \frac{m}{k} \tag{2.3}$$

As it can be seen from equation (2.3), resonant frequency should be made as low as possible for obtaining the high mechanical sensitivity since the sensitivity is inversely proportional to the square of resonant. However, in practice, the value of resonant frequency is bounded by the physical constraints like the finite fracture strength of the used material, manufacturability etc.

Capacitor elements must be added to the above model to obtain a complete model for microaccelerometer system. In this model, movable comb fingers, attached to the proof-mass, and fixed fingers, attached to the moving frame of reference, form the capacitive sensing unit. Figure 2.2a-b shows the simplified schematic of such a capacitive MEMS accelerometer system. Sensing element is a suspended proof-mass at the center of the accelerometer. Under an applied external acceleration, the proof-mass moves with respect to the reference frame, in the influence of spring restoring forces and the damping caused by the motion of air around the moving mass and comb fingers. Consequence of this motion, the value of one capacitance (i.e., C_{s1} or C_{s2}) increases while the other decreases. So, the relative displacement is detected by measuring the differential capacitance change between the movable comb fingers and fixed fingers. In this thesis, single-ended half- bridge configuration, shown in Figure 2.2c, is used as capacitive sense interface. Change in capacitance is measured by applying the high frequency sinusoidal signals to the fixed electrodes and taking the proof-mass as the output node. Capacitance change can occur because of the changing gap (Figure 2.2a) or the changing overlap area (Figure 2.2b) between the movable and fixed fingers.

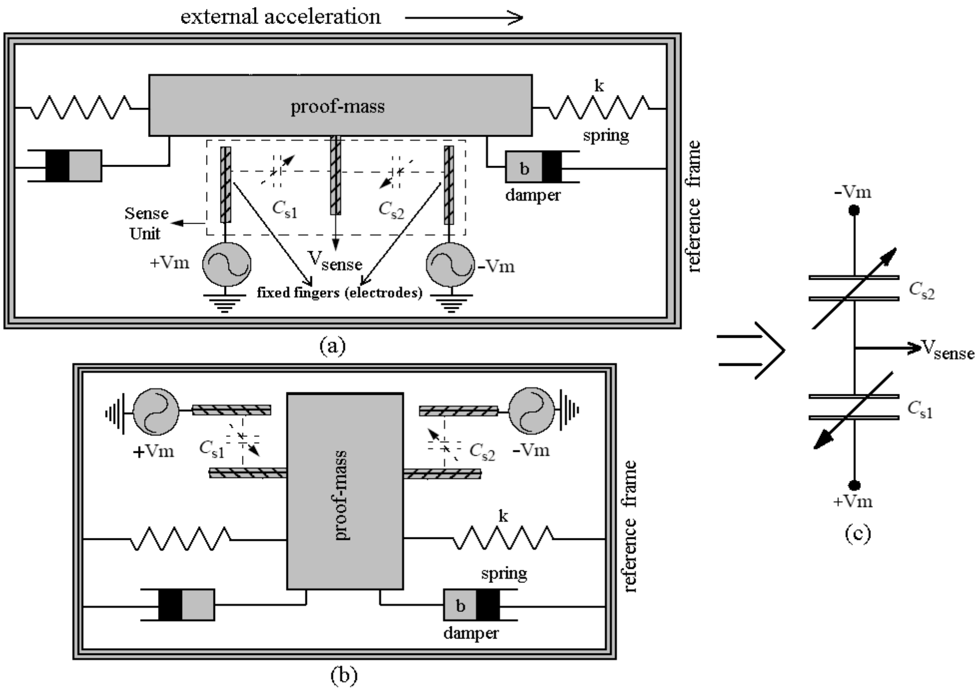

Figure 2.2: Simplified schematic of (a) gap changing (b) overlap area changing MEMS accelerometer (c) and their capacitive equivalence

2.3 Capacitive Position Sensing and Sensitivity

In a micro accelerometer sytem, all the components, shown in Figure 2.2, is realized by using the structural material (polysilicon for this work) of used MEMS process. Simple layout level representation of surface micromachined accelerometer, used in this work, is shown in Figure 2.3. In this topology, number of comb fingers should be made as many as possible to obtain large sense capacitance value since it is very important for the sensitivity of the system (equation (2.19), (2.20)). Damping effect comes into existence because of the motion of air between the movable and fixed structures.

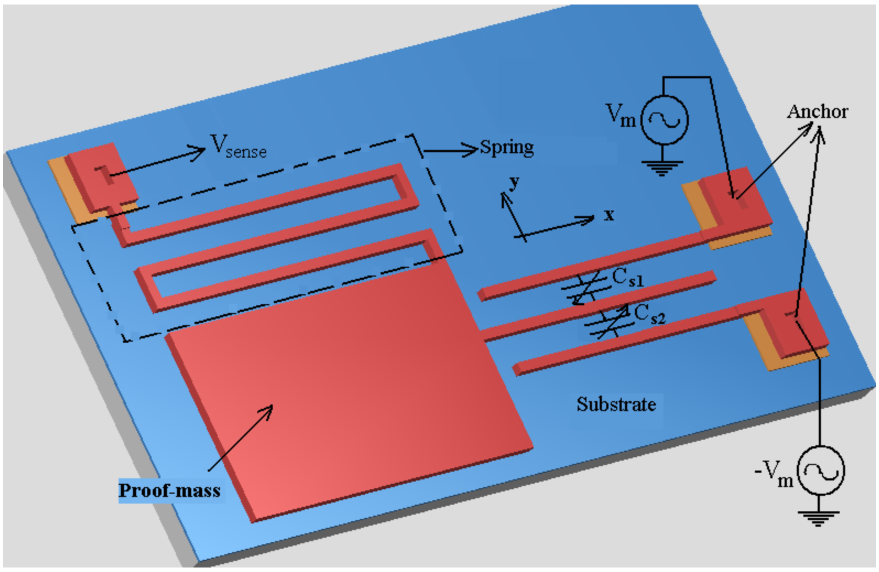

Figure 2.3: Simple layout level representation of surface micromachined accelerometer

For the surface micromachined accelerometers like the one designed in this thesis, capacitive sensing mechanism is attractive since it can be employed both for sensing and actuating purposes. There are a few electronic circuit configurations for capacitive position sense [24]. In this work, charge amplifier circuit is used for measuring the imbalance in capacitances. This interface will be studied in detail in Section 3.4.1. However, the basic concept about the charge amplifier interface is given in this section briefly to obtain the relation between the acceleration and capacitance change. Simplified schematic of the charge amplifier circuit interface with the sense capacitors is shown in Figure 2.4. C_P represents the total parasitic (i.e., undesired) capacitance at the output, components of this capacitance are the capacitance caused by anchors, the capacitance from proof-mass to substrate, and the total capacitance from the electronic sense circuits. These parasitics are very important for voltage divider and Correlated Double Sampling (CDS) pick-off circuit configurations because they cause the considerable attenuation in the output signal [25]. In charge amplifier configuration, the effect of these parasitic capacitances is eliminated since the output node is at virtual ground ($V_X \approx 0$) by the assumption that the gain of operational amplifier is sufficiently high.

When no acceleration occurs, movable fingers of the microaccelerometer are at their rest position (g_0), thus C_{s1} and C_{s2} are equal to their nominal values of C_0 (i.e., $C_{s1}=C_{s2}= C_0$). Under an applied acceleration, C_{s1} increases by ΔC while C_{s2} decreases by ΔC. ΔC changes according to the frequency of the acceleration to which the sensing device is experienced. Upper limit for this frequency is the bandwidth of the micro accelerometer ($\approx f_r$). So, the most generalized definitions of the sense capacitors can be defined as:

$$C_{s1}(t) = C_0 + \Delta C(t) \tag{2.4}$$

$$C_{s2}(t) = C_0 - \Delta C(t) \tag{2.5}$$

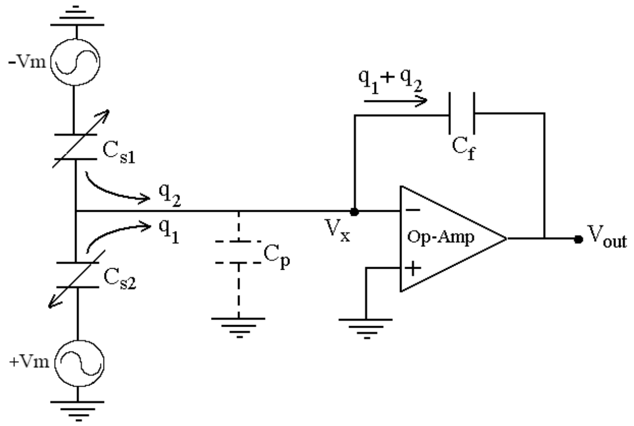

Figure 2.4: Charge amplifier interface for position sense

As it can be seen from the Figure 2.4, at any instant of time, the addition of charges, flowing through the sense capacitors, are equal to the charge on C_f, under the assumption that the operational amplifier is ideal ($V_X \approx 0$). Hence, the voltage signal at the output is defined as:

$$q_1(t) = -V_m(t)C_{s1}(t) = -V_m(t)(C_0 + \Delta C(t)) \tag{2.6}$$

$$q_2(t) = +V_m(t)C_{s2}(t) = V_m(t)(C_0 - \Delta C(t)) \tag{2.7}$$

$$q_1(t) + q_2(t) = V_m(t)[C_{s2}(t) - C_{s1}(t)] = -2V_m(t)\Delta C(t) = V_{out}(t)C_f$$

(2.8)

$$\Rightarrow \; V_{out}(t) = -\left[\frac{2V_m(t)}{C_f}\right]\Delta C(t)$$

As it can be understood from the equation (2.8), at the output of the sense interface Suppressed Carrier- Double Sided Band Amplitude Modulated (SC-DSB AM) signal occurs since the frequency of $V_m(t)$ is much higher ($\approx$200 times in this work) than the bandwidth of $\Delta C(t)$. Also, it is clear that the output voltage is linearly proportional to the capacitance change. To obtain a meaningful measure of acceleration, this signal should be demodulated.

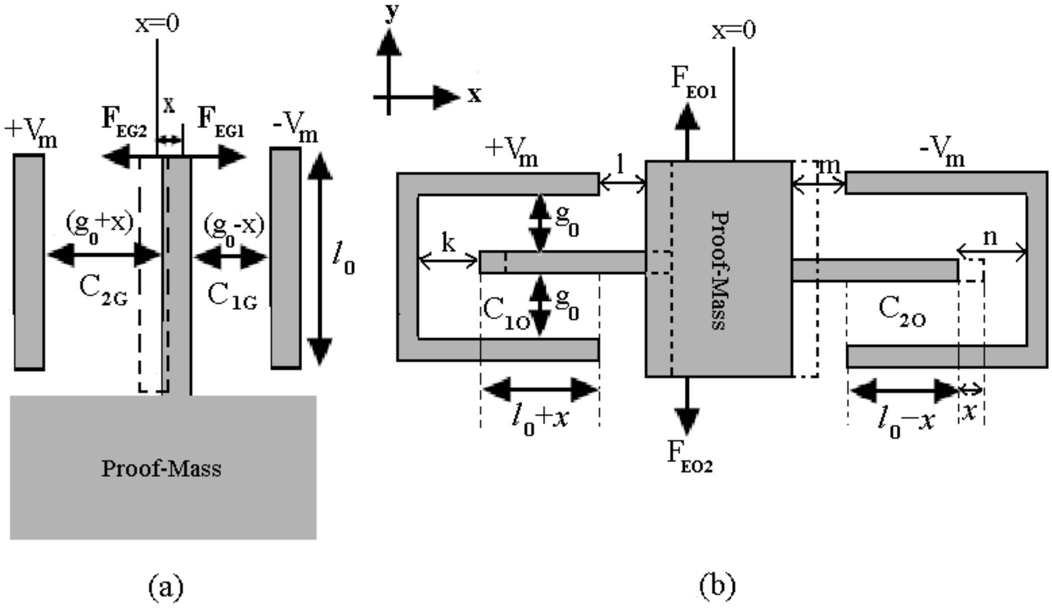

Figure 2.5: Capacitance and spring softening model (a) for gap changing accelerometer (b) overlap area changing accelerometer

To define the acceleration to voltage relation, firstly, we should determine the capacitance change ($\Delta C(t)$) as a function of external acceleration. By using parallel-plate capacitor model, from Figure 2.5a, differantial capacitance change for gap changing accelerometer can be written as:

$$C_{1G}(t) = \varepsilon_0 N_f t_{poly} l_0 \left(\frac{1}{(g_0 - x(t))} \right) \tag{2.9}$$

$$C_{2G}(t) = \varepsilon_0 N_f t_{poly} l_0 \left(\frac{1}{(g_0 + x(t))} \right) \tag{2.10}$$

$$\Delta C_{GC}(t) = C_{1G}(t) - C_{2G}(t) = \varepsilon_0 N_f t_{poly} l_0 \left(\frac{2x(t)}{(g_0^2 - [x(t)]^2)} \right) \tag{2.11}$$

where N_f is the total number of comb fingers, t_{poly} is the thickness of structural layer (poly in this thesis), and ε_0 is dielectric constant of air ($\approx$8.854 10^{-14} F/cm). If we use equation (2.3) for $x(t)$, we arrive the below equation for $\Delta C_{GC}(t)$.

$$\Delta C_{GC}(t) = C_{1G} - C_{2G} = \frac{2m\varepsilon_0 N_f t_{poly} l_0}{k}\left(\frac{a(t)}{(g_0^2 - [ma(t)/k]^2)}\right) \tag{2.12}$$

It is clear that, in general case, the relation between the acceleration and the capacitance change is nonlinear for gap changing accelerometer. For the displacement values much lower than the initial gap ($x(t) << g_0$) equation (2.9), (2.10), and (2.12) can be rewritten as:

$$C_{1G}(t) \approx \varepsilon_0 \frac{N_f t_{poly} l_0}{g_0}\left(1 + \frac{x(t)}{g_0}\right) \tag{2.13}$$

$$C_{2G}(t) \approx \varepsilon_0 \frac{N_f t_{poly} l_0}{g_0}\left(1 - \frac{x(t)}{g_0}\right) \tag{2.14}$$

$$\Delta C_{GC}(t) = C_{1G}(t) - C_{2G}(t) \approx \frac{2m\varepsilon_0 N_f t_{poly} l_0}{k g_0^2} a(t) \tag{2.15}$$

So, when the displacement is small compared to the initial gap (g_0), the relation between the capacitance change and acceleration becomes linear in gap changing accelerometer. For the large displacements the relation will be nonlinear as it is evident from equation (2.12).

If we follow the same way that is used for obtaining the $\Delta C_{GC}(t)$, from Figure 2.5b, differantial capacitance change for overlap area changing accelerometer is found as:

$$C_{1O}(t) = \varepsilon_0 \frac{N_f t_{poly}}{g_0}(l_0 + x(t)) \tag{2.16}$$

$$C_{2O}(t) = \varepsilon_0 \frac{N_f t_{poly}}{g_0}(l_0 - x(t)) \tag{2.17}$$

$$\Delta C_{OC}(t) = C_{1O}(t) - C_{2O}(t) = \frac{2m\varepsilon_0 N_f t_{poly}}{kg_0} a(t) \tag{2.18}$$

If the equation (2.18) is examined, it can be clearly seen that the relation between the acceleration and capacitance change is linear even for large displacements for overlap area changing accelerometer. This is a big advantage compared to the gap changing accelerometer. But one disadvantage of the overlap area changing accelerometer is lower sensitivity than the gap changing one. If we substitute the ΔC value, obtained in equations (2.18) and (2.15), into equation (2.8), the acceleration to voltage sensitivities are found as:

$$S_{GC} = \frac{\partial V_{GC}(t)}{\partial a(t)} \overset{(\frac{ma}{k}=x<<g_0)}{=} \left[-4\frac{m\varepsilon_0 N_f t_{poly}}{C_f kg_0}\right]\left(\frac{l_0}{g_0}\right) V_m(t) = \left(-4\frac{mC_0}{C_f k}\right)\left(\frac{1}{g_0}\right) V_m(t) \tag{2.19}$$

$$S_{OC} = \frac{\partial V_{OC}(t)}{\partial a(t)} \overset{(\text{ for all } \frac{ma}{k}=x)}{=} \left[-4\frac{m\varepsilon_0 N_f t_{poly}}{C_f kg_0}\right] V_m(t) = \left(-4\frac{mC_0}{C_f k}\right)\left(\frac{1}{l_0}\right) V_m(t) \tag{2.20}$$

From equation (2.19) and (2.20), it is seen that, for the accelerometers with the same geometry, the sensitivity of gap changing accelerometer is (l_0 / g_0) times higher than the overlap area changing one. The lower limit for g_0 is constrained by the used technology (2 μm for MUMPS). So, by increasing l_0, the sensitivity of gap changing accelerometer can be made as high as possible. But, it is not possible to obtain the higher sensitivity for overlap area changing accelerometers by using the same method, since its sensitivity is independent of l_0 as it can be seen from the second equality in equation (2.20). Anyway, the capacitance value that must be detected is slightly small (atto Fahrads) for surface micromachined devices so, the lower sensitivity makes the electronic circuit design job more challenging. Because of this reason, overlap area changing accelerometers are not preferred except of a few specific designs [26]. But, as it will be explained in Section 3.2, this disadvantage, defined for overlap area changing accelerometers, will serve as advantage for this work.

2.4 Electrostatic Force Model

The model that is offered in this work requires the force to counterbalance the accelerating force that effects to the gap changing accelerometer to obtain higher dynamic range as explained in detail in Section 3.2. This force should be applied to the movable part to keep it at its central position. For this reason, this mechanism also eliminates the nonlinear effects, which are caused by the large displacements. Because of the small dimensions of micromachined devices, electrostatic force can be utilized for obtaining the restoring forces. Electrostatic force between two charged plates can be defined as:

$$U_E(x) = \frac{1}{2}C(x)[V(t)]^2 \quad \Rightarrow F_E(x) = \frac{\partial U_E(x)}{\partial x} = \frac{1}{2}\frac{\partial C(x)}{\partial x}[V(t)]^2 \tag{2.21}$$

In this work, since the fingers that are used for sensing, are also used to force balance the system, a method should be employed to prevent the interaction between these two signals. The method of frequency domain seperation of the signals is used in this work. From the equation (2.21) it is obvious that the voltage to electrostatic force relation is nonlinear. To linearize the relation, a bias voltage, "V_{bias}", should be applied to one fixed finger and opposite polarity and same magnitude to the other one as shown in Figure 2.6. Additionally, the force balance signal V_f, should be applied to both of the fixed fingers, as a result three different voltages exist at each fixed fingers:

$$\begin{aligned} V_1(t) &= V_m(t) - V_{bias} + V_f(t) \\ V_2(t) &= -V_m(t) + V_{bias} + V_f(t) \end{aligned} \tag{2.22}$$

Assuming no fringe-field effects, the net electrostatic force on the movable fingers is:

$$F_E(t) = F_{E1}(t) - F_{E2}(t) = \frac{\varepsilon_0 N_f t_{poly} l_0}{2}\left(\frac{[V_m(t) - V_{bias} + V_f(t)]^2}{(g_0 - x(t))^2} - \frac{[-V_m(t) + V_{bias} + V_f(t)]^2}{(g_0 + x(t))^2}\right) \tag{2.23}$$

By making the usual assumption that $x(t) << g_0$, equation (2.23) is rewritten as in equation (2.24).

$$F_E(t) = \underbrace{-2\frac{\varepsilon_0 N_f t_{poly} l_0 V_{bias}}{g_0^2}V_f(t)}_{Electrostatic Force} + \underbrace{2\frac{\varepsilon_0 N_f t_{poly} l_0}{g_0^2}V_f(t)V_m(t)}_{High Frequency Component} \tag{2.24}$$

The high frequency component, caused by $V_m(t)$, can be neglected because the sensing element behaves like a mechanical low pass filter. Hence, the electrostatic force is found as:

$$F_E(t) = -2\frac{\varepsilon_0 N_f t_{poly} l_0 V_{bias}}{g_0^2}V_f(t) \tag{2.25}$$

It can be seen that the resulting electrostatic force is a linear function of the balancing (feedforward) voltage for small deflections. The desired dynamic range of the accelerometer system defines the value of the bias voltage. The minimum bias voltage can be calculated by using [31]:

$$V_{bias} = \sqrt{\frac{mag_0^2}{\varepsilon_0 N_f t_{poly} l_0}} \tag{2.26}$$

where a is the maximum acceleration to be compensated by the electrostatic force.

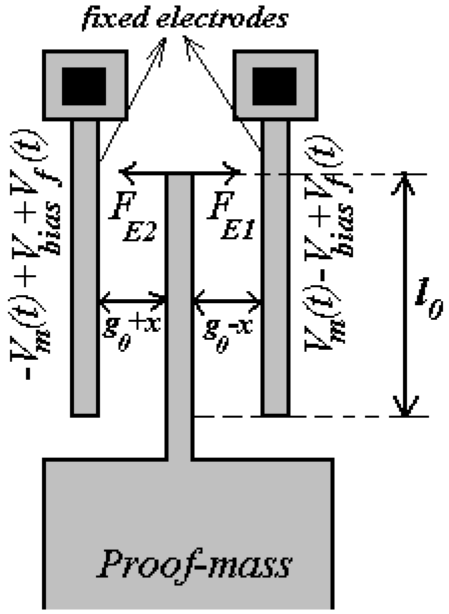

Figure 2.6: Illustration of electrostatic force for gap changing accelerometer

2.5 Electrical Spring Softening Model

In the capacitive sense units of gap changing accelerometer, electrostatic forces are generated on the movable parts as shown Figure 2.5a because of the modulation voltage V_m. So, because of this force, effective spring constant of the system changes from its fixed mechanical value. The net force that effects to all fingers (N_f pieces) is defined as:

$$F_{EGnet}(t) = F_{EG1}(t) - F_{EG2}(t) = \frac{\varepsilon_0 N_f t_{poly} l_0}{2} V_m^2(t)\left(\frac{1}{(g_0 - x(t))^2} - \frac{1}{(g_0 + x(t))^2}\right) \quad (2.27)$$

The effective electrical spring constant is found by differentiating the equation (2.27) with respect to the displacement *x(t)*:

$$k_{EG}(t) = -\frac{\partial F_{EGnet}}{\partial x(t)} = -\varepsilon_0 N_f t_{poly} l_0 V_m^2(t)\left(\frac{1}{(g_0 - x(t))^3} + \frac{1}{(g_0 + x(t))^3}\right) \quad (2.28)$$

$$[V_m(t)]^2 = [V_m \sin(\omega t)]^2 = \frac{V_m^2}{2} + \frac{V_m^2}{2}\sin(2\omega t) \quad (2.29)$$

If equation (2.29) is substituted in (2.27), it is seen that a high frequency and a static force components are generated on the proof-mass since the electrostatic force is proportional with the square of the modulation voltage. The high frequency component can be neglected because the sensing element is a mechanical low pass filter. So, only the static component contributes to the spring softening effect. Moreover, if the static force is sufficiently high, it can cause to latch-up situation in which the proof-mass being attracted and attached to the fixed electrodes. To prevent this situation, amplitude of modulation signal should be selected as small as possible. By assuming small displacements ($x(t) << g_0$) and eliminating the high frequency component of the electrostatic force, effective spring constant for gap changing accelerometer is found as:

$$k_{eff} = k_{mech} + k_{EG} = k_{mech} - \frac{\varepsilon_0 N_f t_{poly} l_0 V_m^2}{g_0^3} \quad (2.30)$$

where k_{mech} is the mechanical spring constant that will be obtained in Section 2.7. Equation (2.1), which is the mathematical model of the accelerometer system, should be written again by taking into consideration the electrostatic effect of modulation signals. The mathematical model of gap changing accelerometer can be rewritten as:

$$m.a_{ext}(t) = m\frac{d^2x(t)}{dt^2} + b\frac{d^2x(t)}{dt^2} + k.x(t) - \frac{\varepsilon_0 N_f t_{poly} l_0}{2} V_m^2(t)\left(\frac{1}{(g_0 - x(t))^2} - \frac{1}{(g_0 + x(t))^2}\right) \tag{2.31}$$

For overlap area changing accelerometer, net force is always *0* along the sensitive axis (i.e., $F_{E01}= F_{E02}$) since the gap between the fingers is not change. And also, if we ignore the side effects due to the *k, l, m, n* distances in Figure 2.5b, there is no net electrostatic force that effects the proof-mass of overlap area changing accelerometer in the sensitive axis, too.

2.6 Viscous Air Damping and Mechanical Noise

Two damping mechanisms form the damper component of the accelerometer, one is structural damping which is caused by the friction within the movable structural layer and the other is viscous air damping caused by the flow of the air molecules around the movable parts of the system. Structural damping can be ignored because it is sufficiently lower than the viscous air damping for the devices that operate at atmospheric pressures. Couette-flow damping and the squeeze film damping are the two main components of viscous air damping for comb drive type accelerometers used in this work. Coutte-flow damping comes from the shear flow of air between parallel plates. For example, the air flow between the substrate and movable structures of accelerometers (proof-mass + comb fingers + springs) for our design. The damping coefficient of Couette-flow is determined as:

$$b_{Couette} = \mu \frac{A}{d_f} \tag{2.32}$$

where d_f is the air film thickness, μ is the viscosity of air, and A is the overlapping area of parallel plates.

The changing air gap, between the two closely placed parallel plates as shown in Figure 2.7, is the reason of the squeeze film damping. For the micromachined devices, the behavior of the squezee films is defined by [27] with the below differantial equation.

$$\frac{\partial}{\partial x}\left[\left(\frac{\rho h(t)^3}{\mu}\right)\frac{\partial P(x,y)}{\partial x}\right]+\frac{\partial}{\partial y}\left[\left(\frac{\rho h(t)^3}{\mu}\right)\frac{\partial P(x,y)}{\partial y}\right]=12\frac{\partial[\rho h(t)]}{\partial t} \tag{2.33}$$

where P is the film pressure, ρ is density, μ is the viscosity of air, h is film thickness, and x and y are the coordinates along the motion of the film. By using equation (2.33) squeeze film damping coefficient for a rectangular plate is found in [27] as:

$$b_{squeeze} = f\left(\frac{W}{L}\right)\frac{\mu W L^3}{g_0^3} \tag{2.34}$$

where *f(W/L)* is given in Figure 2.8 [27]. For the gap changing accelerometer, designed in this work, the squeeze film damping occurs between the fixed and movable comb fingers and it changes to Hagen-Poiseuille flow because the air gap between the fingers is narrow when compared with the finger dimensions [28]. Total damping coefficient for Hagen-Poiseuille flow between the fingers is defined as:

$$b_{Hagen-Poiseuille} = 7.2\mu N_f \frac{l_0 t_{poly}^3}{g_0^3} \tag{2.35}$$

where N_f is the total number of comb fingers, l_0 is the finger length, t_{poly} is the finger thickness, and g_0 is initial gap between the fingers. If we assume that the velocity of the beams in the spring is half of the velocity of the proof-mass on average [28], the total damping coefficient for comb finger type accelerometers can be written as:

$$b_{total} = b_{Couette} + b_{Hagen-Poiseuille} = \mu\frac{(A_{proof-mass} + N_f A_{comb\,finger} + 0.5A_{spring})}{d_f} + 7.2\mu N_f \frac{l_0 t_{poly}^3}{g_0^3} \tag{2.36}$$

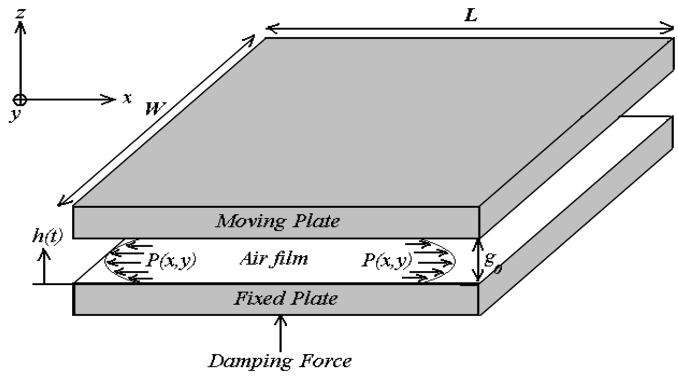

Figure 2.7: Schematic illustration of squeeze-film damping mechanism

The random collision of the air molecules with the movable structures causes to mechanical thermal noise, which is also named as Brownian noise. This is a very important performance parameter since the addition of it and the electronic noise from the front-end circuits determine the minimum detectable acceleration level. Spectral density of input referred Brownian noise equivalent acceleration is:

$$\sqrt{a_{Brownian}^2} = \frac{\sqrt{4k_B Tb}}{m}\sqrt{\Delta f} = \sqrt{\frac{4k_B T\omega_r}{mQ}}\sqrt{\Delta f} \tag{2.37}$$

where k_B is Boltzman's constant (*1.38066x10^{-23} J/K*), T is the ambient temperature, b is the damping factor and Q is the quality factor. Vacuum packaging can reduce damping (so, the Brownian Noise) and increase the quality factor significantly.

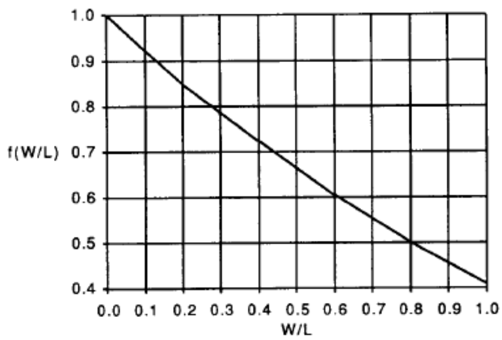

Figure 2.8: Effect of aspect ratio on damping produced by rectangular plate [27]

2.7 Spring Stiffness Model

Spring constant is one of the most important performance parameter of the accelerometer system. As it is obvious from equation (2.3), it determines the mechanical sensitivity and resonance frequency of the system. For this reason the stiffness of the system should be modeled accurately. Due to the rigidity of proof-mass, polysilicon folded beams dominates in the stiffness model of our design. For the small deflections springs that are made of rectangular polysilicon beams, are modeled as linear but for the large displacements force to displacement relation begins to become nonlinear. In the literature, there are a few topologies for spring design like clamped-clamped flexure, folded flexure, crableg flexure, and serpentine flexure. We used serpentine flexure topology to implement the springs of the designed accelerometers since it is linear over the wide range of displacement values.

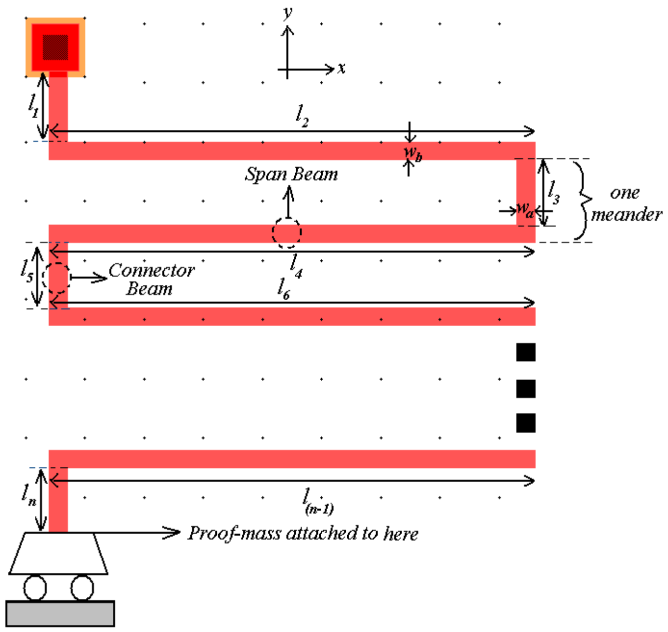

Figure 2.9: Schematic of polysilicon serpentine spring

The schematic of the serpentine spring is shown in Figure 2.9. The meandering snake-like shape of the beam segments causes the spring to be named as serpentine. The beams that form the width of the meanders are called span beams and the other beams called connector beams since they connect the span beams. In our design, all the connector beams have the same dimensions ($l_1= l_3= l_5\ldots\ l_n= l_a$), and also all the span beams have the same dimensions ($l_2= l_4= l_6\ldots\ l_{n-1}= l_b$), too. We derive the effective spring constant of the one serpentine flexure by using energy methods as described in [29]. To utilize this method, a force (F) or a moment (M) is applied at the movable end of the spring at the desired direction, and by using Castigliano's second theorem and boundry conditions, the displacement δ at the load point is found. Then, the spring constant is found from the Hook's Law ($k=F/\delta$). A free body diagram of the serpentine spring with *n* meanders is shown in Figure 2.10. The index of the connector beams changes from *i=1* to *n* and the index of span beams changes from *i=1* to *n-1*. The total strain energy of a linear structure is calculated by using:

$$U = \sum_{i=1}^{n} \int_{0}^{L_i} \frac{M_i(\xi)^2}{2EI_i} d\xi \tag{2.38}$$

where $M_i(\xi)$ is the bending moment along the *i'*th beam, *E* is the Young's Modulus of beam material, L_i is the length of the *i*'th beam in the serpentine spring, and ξ is the distance from the related beam end. According to Castigliano's second theorem, the derivative of the strain energy *U* is taken with respect to the applied force F_j to find the displacement (δ_j) at the point where the force is applied. Analytic expression of this theorem is written as:

$$\delta_j = \frac{\partial U}{\partial F_j} \tag{2.39}$$

Similarly, to calculate the the angular displacement, θ_j, the derivative is taken with respect to applied moment M_j, so it is defined as:

$$\theta_j = \frac{\partial U}{\partial M_j} \tag{2.40}$$

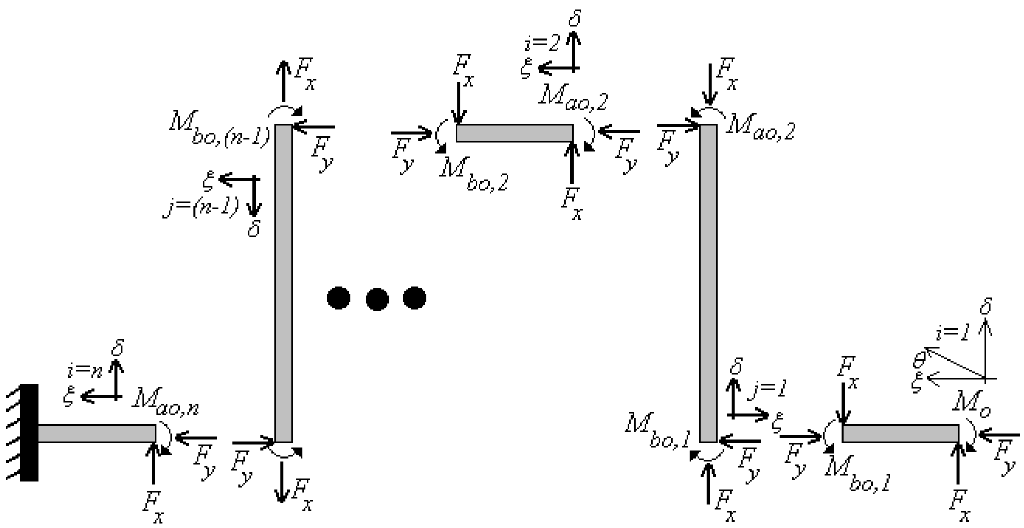

Figure 2.10: Free body diagram of one serpentine spring (Adapted from [29])

From the free body diagram in Figure 2.10, moment of the each beam is written as:

$$M_{a,i} = M_o - F_x[\xi + (i-1)l_a] - \left(\frac{1+(-1)^i}{2}\right)F_y l_b \quad ; \quad i = 1,...,n \tag{2.41}$$

$$M_{b,j} = M_o - jF_x l_a + F_y\left[(-1)^j \xi - \left(\frac{1+(-1)^j}{2}\right)l_b\right] \quad ; \quad j = 1,...,n-1 \tag{2.42}$$

By using equation (2.41) and (2.42) the total strain energy of the serpentine spring is:

$$\begin{aligned} U = & \sum_{i=1}^{n}\int_0^{l_a}\left[M_o - F_x[\xi + (i-1)l_a] - \left(\frac{1+(-1)^i}{2}\right)F_y l_b\right]^2 \frac{1}{2EI_{z,a}}d\xi \\ & + \sum_{i=1}^{n-1}\int_0^{l_b}\left[M_o - jF_x l_a + F_y\left[(-1)^j \xi - \left(\frac{1+(-1)^j}{2}\right)l_b\right]\right]^2 \frac{1}{2EI_{z,b}}d\xi \end{aligned} \tag{2.43}$$

$M'_{b,j}$ is used in place of $M_{b,j}$ in [29] to simplify the calculation of the second integral in equation (2.43).

$$M_{b,j} \approx M'_{b,j} = M_o - jF_x l_a - F_y \xi \, ; \quad j = 1,...,n-1 \tag{2.44}$$

When determining the x-directed spring constant, the boundry conditions that are used for the calculation of the unknown variables (F_x, M_o and δ_x) are:

$$\delta_y = \frac{\partial U}{\partial F_y} = 0 \tag{2.45}$$

$$\theta_o = \frac{\partial U}{\partial M_o} = 0 \tag{2.46}$$

$$\delta_x = \frac{\partial U}{\partial F_x} \tag{2.47}$$

After obtaining F_x and M_o from the boundary conditions given above, total strain energy is calculated by substituting them in equation (2.43) and by solving the integrals. Then x directed spring constant calculated from equation (2.47) as in equation (2.48) and (2.49).

$$For\ even\quad n,$$

$$k_x = \frac{F_x}{\delta_x} = \frac{12EI_{z,b}\{(3a'+l_b)n-l_b\}}{l_a^2 n\{(3(a')^2+4a'l_b+l_b^2)n^3-2l_b(5a'+2l_b)n^2+(5l_b^2+6a'l_b-9(a')^2)n-2l_b^2\}} \tag{2.48}$$

$$k_x = \frac{F_x}{\delta_x} = \frac{12EI_{z,b}}{l_a^2 n\{(a'+l_b)n^2-(3n-2)l_b\}} \qquad For\ odd\quad n, \tag{2.49}$$

where $a' \equiv \left(\dfrac{I_{z,b}\, l_a}{I_{z,a}}\right)$. A similar procedure by using the boundry conditions,

$$\delta_x = \frac{\partial U}{\partial F_x} = 0 \tag{2.50}$$

$$\theta_o = \frac{\partial U}{\partial M_o} = 0 \tag{2.51}$$

gives the *y*-directed spring constant as:

$$For\ even\quad n, \tag{2.52}$$

$$k_y = \frac{F_y}{\delta_y} = \frac{12EI_{z,b}\{(a'+l_b)n^2-(3n-2)l_b\}}{l_b^2\{(3(a')^2+4a'l_b+l_b^2)n^3-2l_b(5a'+2l_b)n^2+(5l_b^2+6a'l_b-9(a')^2)n-2l_b^2\}}$$

$$k_y = \frac{F_y}{\delta_y} = \frac{12EI_{z,b}\{(a'+l_b)n-l_b\}}{l_b^2(n-1)\{(3(a')^2+4a'l_b+l_b^2)n+3(a')^2-l_b^2\}} \quad \text{for odd n,} \tag{2.53}$$

The moment of inertia of the rectangular beams, used in our design, is given by:

$$I_{z,a} = \int_{-t_{poly}/2}^{t_{poly}/2}\int_{-w_a/2}^{w_a/2} x^2\,dx\,dz = \frac{t_{poly}w_a^3}{12} \tag{2.54}$$

$$I_{z,b} = \int_{-t_{poly}/2}^{t_{poly}/2}\int_{-w_b/2}^{w_b/2} x^2\,dx\,dz = \frac{t_{poly}w_b^3}{12} \tag{2.55}$$

The axial stress comes out during the fabrication process of the polysilicon sensors as a result of the different thermal coefficients of the deposited polysilicon films and the other films. This stress causes nonlinearity in spring constant especially in springs formed by single beam and in clamped-clamped flexures. Analytical model of the nonlinear force-displacement relation is well studied in [30].

3 DESIGN OF FEEDFORWARD MEMS ACCELEROMETER

3.1 Introduction

The parameters of the mechanical systems, described in Section 2, can be found by using the Finite Element Analysis (FEA) software packages, but at the optimization level of the design, this is not reasonable since it is a time consuming job. For this reason, the calculation of the parameters from the derived analytical models is preferred at this level of the design. After the optimization, more accurate values can be found from the FEA simulation results. So, by using the analytic models, obtained in Section 2, we realized a PC programme in a visual software development environment (C++ Builder) to obtain the mechanical and electrical parameters for the desired accelerometer system. Figure 3.1 shows some screen views from this software. The software is named as MEMS Accelerometer Behavioral Modeling Software (MABEMS). By entering the physical design variables like geometric dimensions and some electrical variables, all the parameters are found by the software automatically in a short time. This software finds the spring constant for three types of spring topologies; Crab-leg Flexure, Folded Flexure, and Serpentine Flexure. In addition to the numeric values, the phase and the amplitude responses can be displayed in a graphical environment. We optimized our accelerometer system by using this software and then, compared with FEA simulation results.

The ultimate goal of this work is to complete the design of MEMS accelerometer system, which uses the force feedforward method as an alternative to the conventional closed-loop force feedback accelerometers. Main advantage of this offered method is the high dynamic range. In addition, it has the advantage of better linearity, and no latch-up mechanism, caused by the feedback voltages. The other advantages will be explained further sections. We used MATLAB Simulink simulations for the behavioral level modeling of the full system. Then by using the lumped parameter model of the mechanical device, Pspice simulations are carried out by combining the mechanical and electrical interface in the same environment.

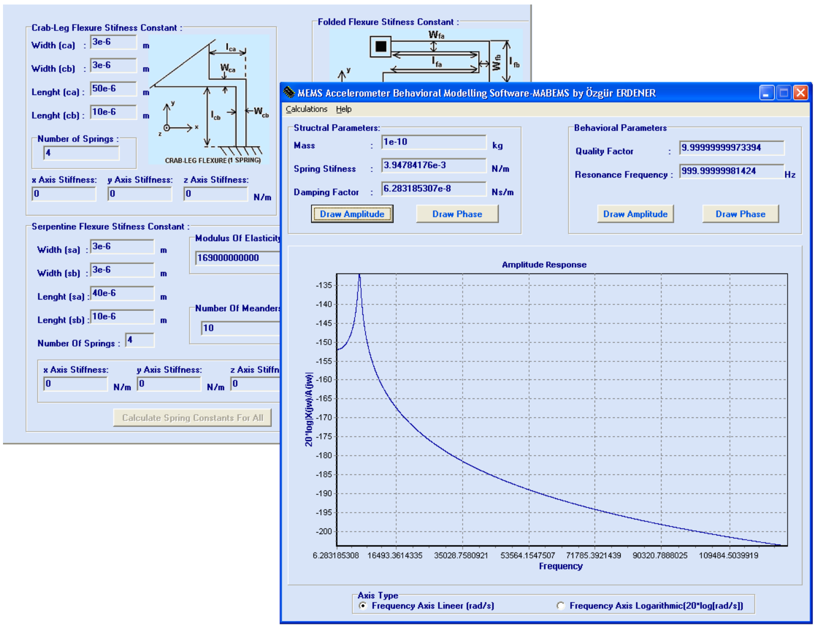

Figure 3.1: Screen views from the software, realized for the lumped parameter calculations (MABEMS)

3.2 Force Feedforward Mechanism

Accelerometers, operated in openloop, have limited bandwidth, linearity and dynamic range. Additionally, non-linear effects caused by the large displacement of the proof-mass are dominant in open loop designs. To overcome these problems, conventional methods use the sensing element in a closed loop control system. In this method, proof-mass is kept at its initial position between the fixed fingers by applying a feedback force. So, the output of the system is force feedback signal, which is utilized for counterbalance the external accelerating force. Consequently, feedback signal is employed as a measure for acceleration in this method. As it can be understood from the above explanations for the closed loop system, sensitivity and bandwidth of the sytem can be directly determined by the force feedback loop. According to the application, the closed loop control can be implemented with either analog feedback [9, 31] or a digital sigma-delta feedback loop [18, 32].

The principal block diagrams of analog and digital closed loop designs are shown in Figure 3.2. The digital closed loop sytem is preffered to analog closed loop system since the feedback force is always linear function of the output voltage. As we discussed in section 2.4 electrostatic forces become nonlinear for large displacements of the proof-mass in analog methods. Compensation blocks are required in feedback loop to ensure the stability of the system. This compensators are used to add a left half-plane zero to the transfer function of the closed-loop system for decreasing the phase delay at the frequency of unity gain.

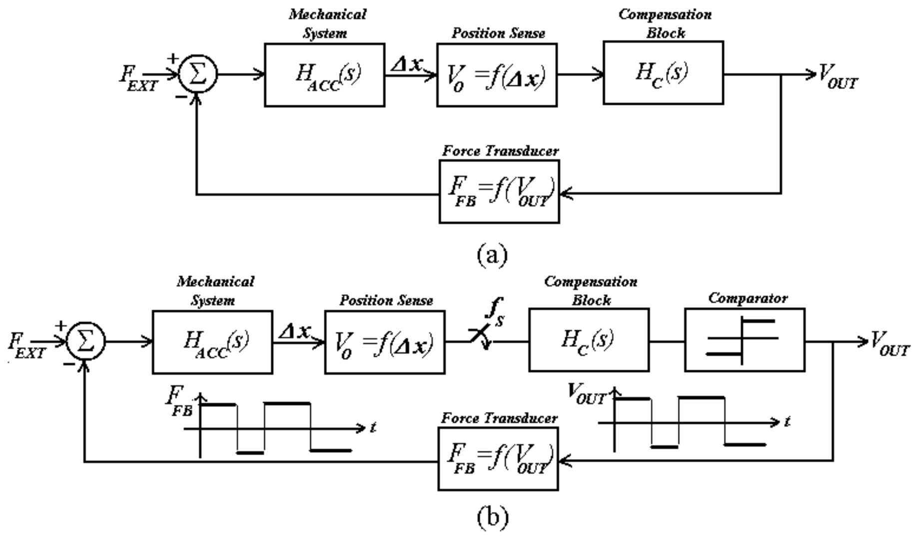

Figure 3.2: Principal block diagram of accelerometers with (a) analog force feedback loop and (b) digital force feedback loop

As it was known, resolution of the designed systems is not infinite because of the physical constraints like noise level, component nonidealities etc. For the MEMS accelerometers, the resolution of the system is defined as minimum detectable acceleration step. To increase the resolution of the accelerometer, sensitivity[1] should be made as high as possible since the noise level of the designed electronic and mechanical interface is almost fixed. Dynamic range, which is the ratio of the maximum detectable acceleration to minimum detectable acceleration, is the main performance parameter for accelerometers. In general, dynamic range of the accelerometers remains fixed, even in closed loop designs, since they could be designed to measure high but rougher accelerations or low but more precise accelerations.

We offer a new method, named as "*Force Feedforward Mechanism*", to extremely increase the dynamic range of the system. Principal block diagram of this method is shown in Figure 3.3. There are two separate mechanical devices in this system such that the overlap area changing design always forms the dynamic offset of the gap

[1] We mean voltage to acceleration sensitivity since this definition includes the sensitivity of both the electronic and mechanical interface.

changing design. Feedforward force from the overlap area changing accelerometer is applied to the proof-mass of the gap changing design to keep it at the vicinity of central position between the fixed fingers (so it is always linear because of the small displacements). As we discussed in Section 2.3, since the sensitivity of the gap changing design is much higher than the overlap area changing design, more precise acceleration values can be measured by gap changing design while the rougher values are measured by overlap area changing design. For example, we assume that the minimum detectable acceleration step (resolution) is 1 g for overlap area changing design and 0.09 g (this ratio is true for this work) for gap changing design. If the external acceleration is 200.19 g, 200g of this value is measured by the overlap area changing design and feedforward force that corresponds to this acceleration value is applied to the gap changing design. So, the input acceleration for the gap changing design becomes the difference between the external acceleration and the acceleration equivalence of the feedforward force from overlap are changing design. Namely, the input acceleration for gap changing design is 0.19 g. Because of its limited resolution, this value is measured as 0.18 g by gap changing design. Finally, to find the external acceleration precisely, the measured values from the overlap area changing design and gap changing design can be evaluated separately or two signals can be summed if the system is well calibrated. It is obvious from the explanation of the force feedforward mechanism that the overlap area changing accelerometer should be linear even for large displacements since it operates in openloop. We had proven in Section 2.3 that the overlap area changing design is always linear. If we generalize the definition of the *"Force Feedforward Mechanism"*:

- The less sensitive system forms the dynamic offset[2] of the more sensitive device. The rougher value of the input signal is measured by the less sensitive system and a feedforward signal, formed by it, is applied to the more sensitive system. So, the input to the more sensitive system is the precision part of the real input signal and it is measured by this system. At the output this two signals summed. So the dynamic range of the system can be increased by separately optimize the sensitivity of the both system.

[2] Since this offset value changes with the input signal, we named it as *"dynamic offset"*.

From the explanation of the mechanism, it is seen like that it has the same mechanism with the closed loop operation. But the difference is at the dynamic behaviour. In the closed loop systems there is latch up risk at shock acceleration conditions caused by the feedback force. But this is not valid for force feedforward design since there are two separate sytems. Since there is no spring softening effect and nonlinearity for overlap area changing design (Section 2.5), maximum detectable acceleration for this system, is infinite (theoricaly, but in reality it is limited by the geometric parameters and electrical signal levels). So, the dynamic range of the overall system can be made extremely high by using force feed forward mechanism in appropriate designs. The main disadvantage of this mechanism is the requirement for two mechanical devices, which causes more area occupation and two separate position sense circuit.

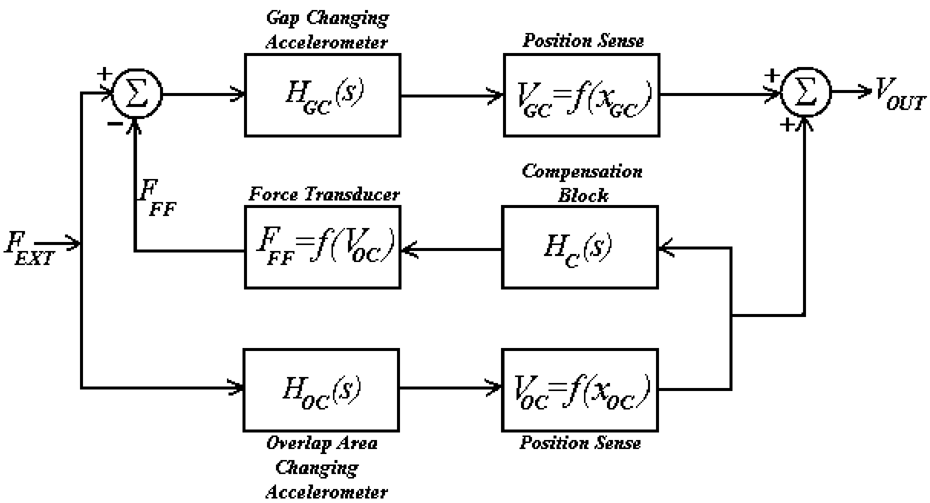

Figure 3.3: Principal block diagram of offered analog force feedforward accelerometer system

3.3 Design of Mechanical Structures

3.3.1 Description of Mechanical Devices and Main Considerations

As it is stated in section 3.2, our system includes two seperate mechanical device in comb finger topology. One of this systems utilizes the changing gap for capacitive position sense interface while the other utilizes changing overlap area. To realize such a system the direction of the comb fingers must be made perpendicular to each other while the devices are located on the substrate. The layout of the designed accelerometers is shown in Figure 3.4. The sensitive axis is *y*-axis for this design. In

Figure 3.4, the device, numbered with “1”, is gap changing accelerometer and the device, numbered with “2”, is overlap area changing accelerometer. All the structural parts are designed with POLY1 layer of MUMPS process, which has the thickness of *2 μm*. POLY0, is used as conductive lines for the electrical connection and also it is utilized as the substrate ground electrode to prevent the floating capacitances between the substrate and movable parts of the system. So, all the movable parts have the ground electrode underneath. The stack of layers, formed by poly and metal, are used in bonding pads. Total area (including bond pads) of the design is *1552 μm x 851 μm*. Effective area, including fixed fingers and springs, of gap changing accelerometer is *541 μm x 652 μm* and, overlap area changing accelerometer is *898 μm x 424 μm*.

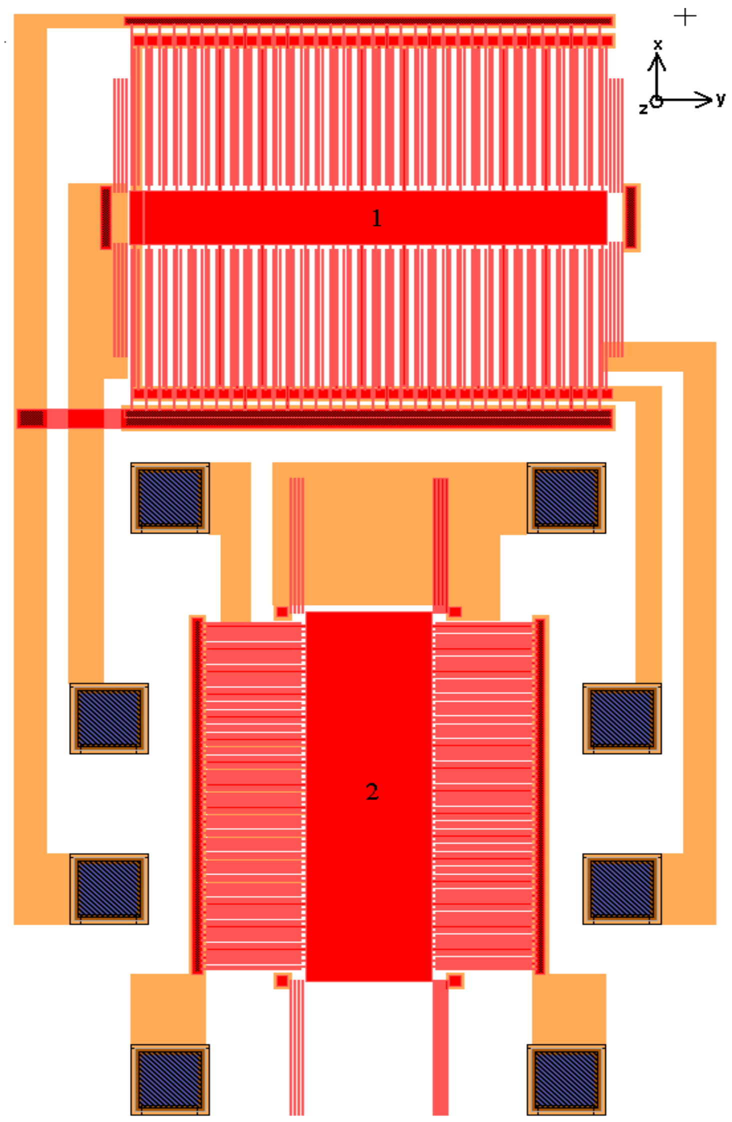

Figure 3.4: Layout of designed accelerometers

Both of the devices are fixed to the substrate by the means of four serpentine springs, which are attached to the end corners of the proof-masses. To obtain the high sensitive devices, masses should be made as much as possible and the spring constants as small as possible (Section 2.3). Since the thickness of the structural material is fixed to $2\ \mu m$ by the Technology, only the area of the proof-mass can be manipulated to obtain the heavier devices. Resistance to the out-of-plane and in-plane shock accelerations gets lower if the mass gets higher and if the spring constant gets lower. In shock cases, the maximum stress must be lower than the Fracture Strenght of the structural material to prevent the cracking of the mechanical devices. FEA[3] results show that the maximum stress for *1500 g* in-plane acceleration, is *92.32 MPa* for gap changing accelerometer and *167.18 MPa* for overlap area changing accelerometer. These values are well below the fracture strenght of the polysilicon (*1.2 GPa* for MUMPs). As it can be seen from Figure 3.5, the maximum stress values occur at the connection points of the connector and span beams of the serpentine spring. Since the proof-masses are wide and large plates, etch holes (with dimensions $3\mu m \times 3\mu m$) are placed on them to guarantee the complete release of the movable structures. The distance between the proof-mass and substrate is $2\mu m$. From the FEA results, it is seen that the out-of-plane accelerations higher than *282 g* for gap changing and *119 g* for overlap area changing accelerometer, can cause the proof-masses to stick to the substrate. To prevent this situation, the contact area of the two surfaces should be made low. For this reason, dimples are placed on the proff-masses. One another important parameter for the sensitivity is capacitance between the fixed and movable comb fingers. From the parallel plate capacitance model, given in equation (2.15), it is seen that to increase the capacitance, the only variable that can be manipulated is lenght of the comb fingers (it must be noted here again, this is not the case for overlap area changing accelerometer) since the thickness is fixed by technology and minimum gap and number of fingers are limited by the technology design rules. But if the lenght of the comb fingers are made very long, curling of the fingers can occur because of the residual stresses in poly that occur during the process. Also these long comb fingers attached to the rigid body (i.e., proof-mass) can be curled because of the high accelerations and this can cause

[3] In this work, a commercial FEA simulation package named ANSYS® is used. In mechanical simulations, structure is meshed by using 3-D 10-Node Tetrahedral Structural Solid (Solid 187 element).

nonlinear capacitance effects. As it can be seen from the Figure 3.6, maximum displacement of one comb finger, which have *200 μm* lenght, is *0.296 μm* for *1500 g* acceleration. Accelerometers are designed by taking these topics into consideration. The mass of the gap changing accelerometer is *0.34 μg* and overlap area changing accelerometer is *0.53 μg*. Gap changing accelerometer has *68* fingers with the lenght of *200 μm*. Overlap area changing accelerometer has *122* fingers with the lenght of *126 μm*.

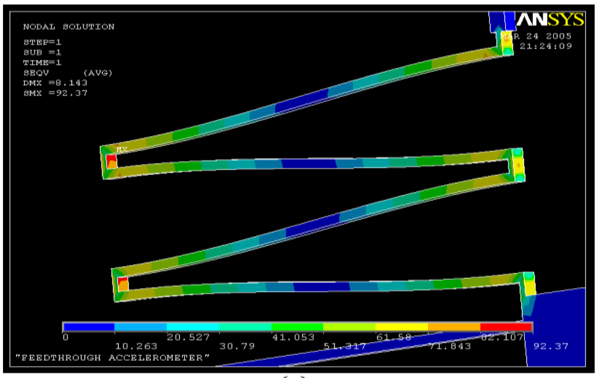

(a)

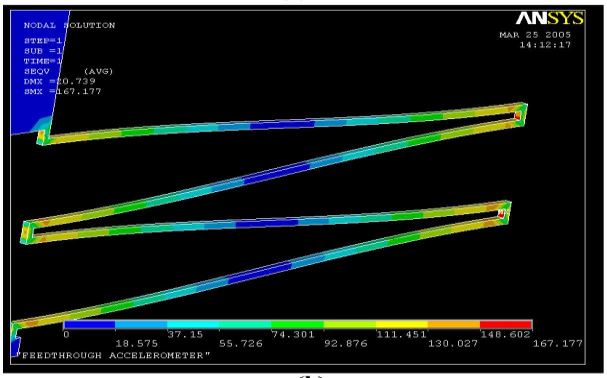

(b)

Figure 3.5: Stress distribution (for 1500 g acceleration) on the serpentine springs of (a) gap changing (b) overlap area changing accelerometer

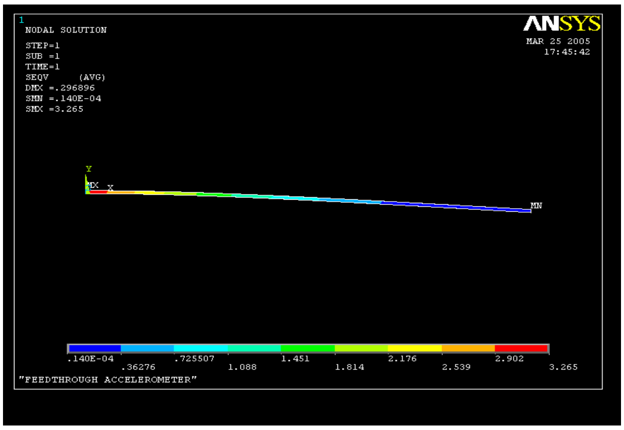

Figure 3.6: Curling of one comb finger (200 μm long) for 1500 g acceleration

3.3.2 Spring Constants

Since the sensitivity of the accelerometer is inverseley proportional to the spring constant, spring design is the most important level of the design process. Four serpentine spring is used at both of the accelerometers, in this work. The dimensions of the springs are optimized by using the MABEMS software. Since the sensitivity of the overlap area changing accelerometer is inherently well below the sensitivity of the gap changing accelerometer (Section 2.3), to compensate this situation at a certain rate, spring constant of the overlap area changing accelerometer is made lower than the other. Springs are formed by using 5 connector beams and 4 span beams. In gap changing accelerometer, connector beams have 2 μm width, 3 μm lenght and the span beams have 2 μm width, 160 μm lenght. In overlap area changing accelerometer, the dimensions are the same except that the lenght of span beams are 190 μm. By using these dimensions in MABEMS, the spring constants and resonance frequencies, for sensitive axis, are found. The obtained values are given in Table 3.1.

Table 3.1: Calculated spring constants and resonance frequencies in sensitive axis

	Gap Changing Design	**Overlap Area Changing Design**
Spring Constant	0.617 N/m	0.372 N/m
Resonance Frequency	6783 Hz	4225 Hz

FEA simulations are carried out to determine the resonant mode shapes and frequencies of the devices. Since the meshing of the complex structures is time consuming process, the etch holes are lumped together into one large hole in the middle of the proof-masses. Figure 3.7 and Figure 3.8 shows the results for first 4 weakest modes of the both design. The modes are at 6208, 6847, 8706, and 11588 Hz for gap changing design and 4011, 4233, 5016, and 8071 Hz. for overlap area changing design. The second modes are the desired modes of vibration in the *y*-axis. The first modes are vibration in the *z*-axis and the third and fourth modes are torsional. So, the resonant frequency in the sensitive axis, found by FEA simulation, is 6847 Hz. for gap changing and 4233 Hz. for overlap area changing accelerometer. If the values in Table 3.1 are compared with the FEA results, it is seen that the results, obtained from the analytical model, derived in Section 2.8, are in well agreement with the finite element analysis results.

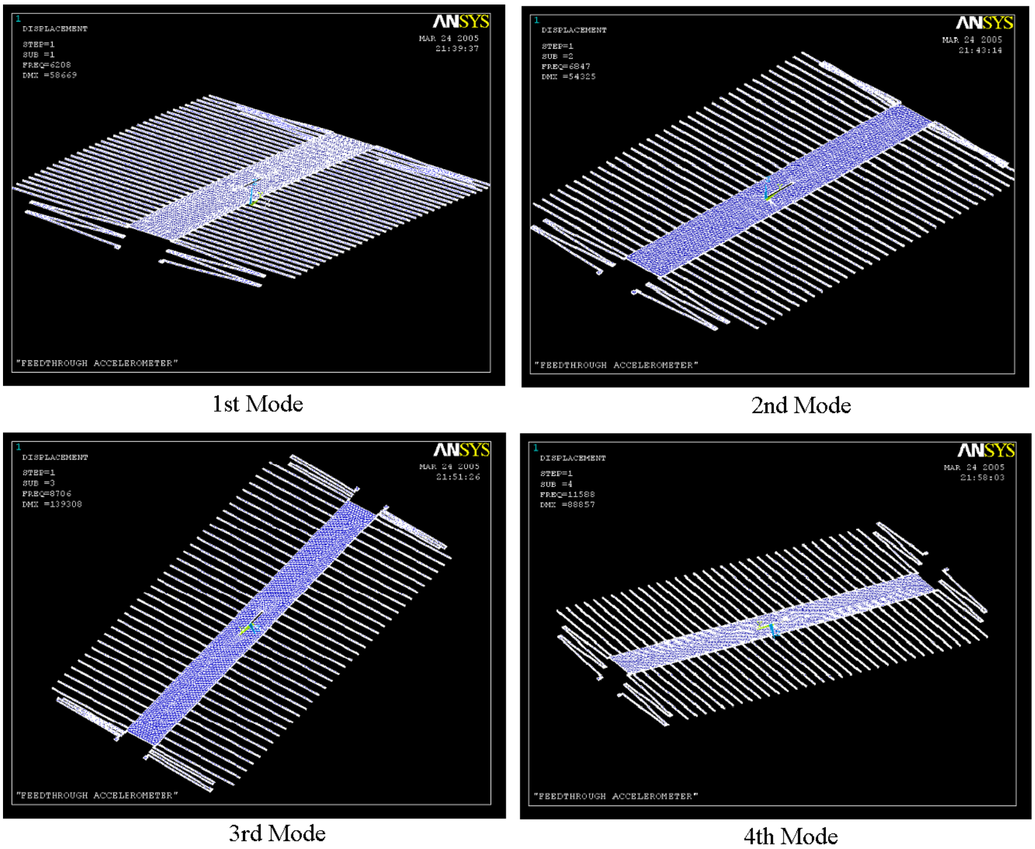

Figure 3.7: Mode shapes of the gap changing accelerometer

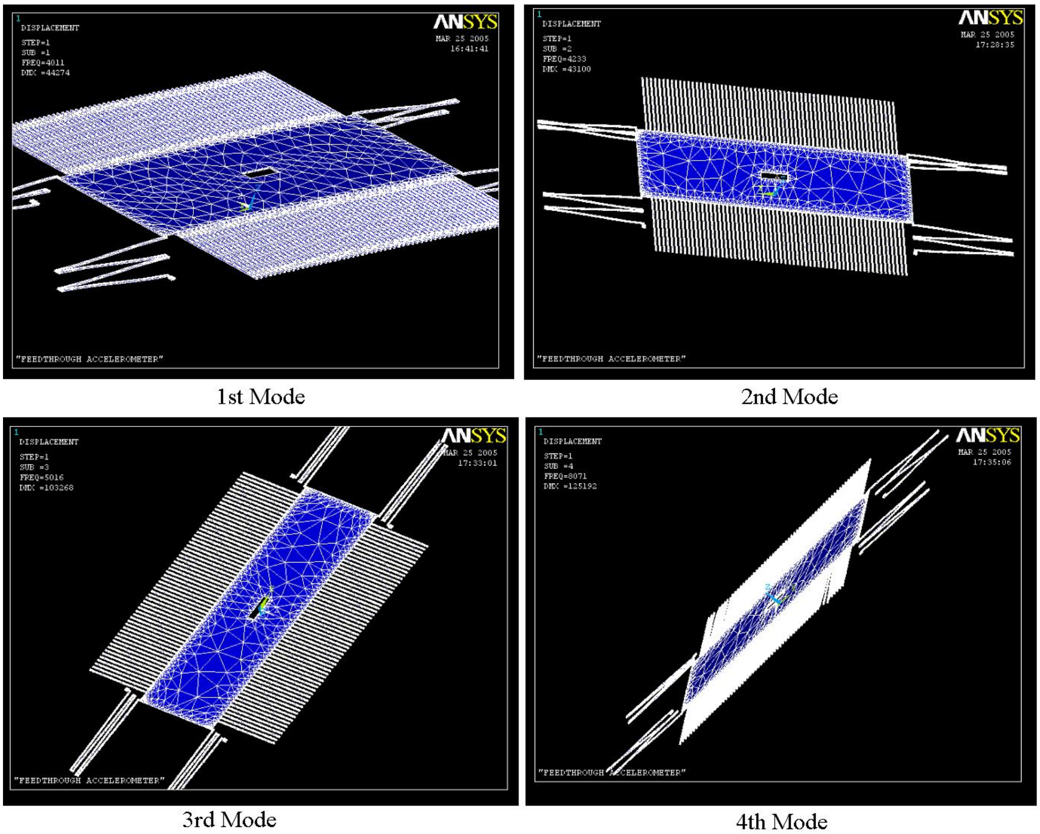

Figure 3.8: Mode shapes of the overlap area changing accelerometer

As we explained in Section 2.5, spring softening effect occurs in gap changing accelerometer because of the modulation signals in capacitive sensing unit. This mechanism determines the upper limit for amplitude of modulation signals (V_m). In the mean time, this amplitude is linearly propotional with the acceleration to voltage sensitivity (equation (2.19), (2.20)). For these reasons, optimum value for the amplitude of modulation signals is determined by taking these two effects into consideration. As it can be seen from Table 3.1, the mechanical spring constant (i.e., k_{mech}) for gap changing accelerometer is 0.617 N/m. Figure 3.9 (Drawned by MABEMS) shows the variation of equivalent spring constant (i.e., $[k_{mech+}\ k_{EG}(x)]$) with displacement by taking the amplitude of modulation voltage as parameter. When the curve, corresponds to 1 volt, is examined, it is seen that the effective spring constant goes below zero[4] for the displacements higher than ± 1.43 μm. For the displacements lower than ± 0.5 μm, effective spring constant nearly remains constant at value 0.586 N/m. Because of the force feed forward mechanism, displacements of the gap changing accelerometer stays small during the operation of the system. So, in this design, the amplitude of the modulation voltages for the gap changing accelerometer is selected *1 Volt*. Since the overlap area changing accelerometer is not effected from the spring softening mechanism, amplitude of the modulation signals is selected *2 Volts* to make the sensitivity higher.

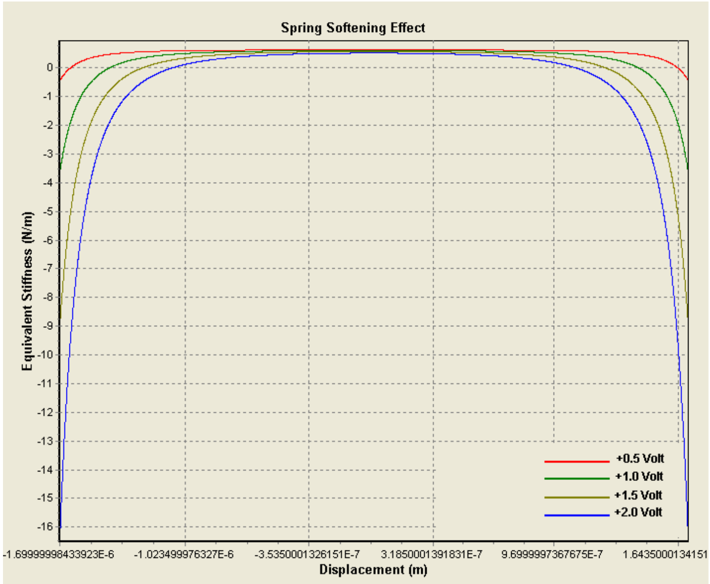

Figure 3.9: Spring softening effect for gap changing design

[4] This means negative spring constant and causes to latch-up condition. To recover the system from this situation, it must be powered off and on again.

3.3.3 Damping Coefficients and Brownian Noise

Dominant component of the damping mechanism for gap changing design comes from Hagen-Poiseuille flow, which is described in Section 2.6. However, Coutte-flow damping, caused by the motion of the air between the proff-mass and substrate, is also important for this design. Since there is almost no squeezing film along the sensitive axis of the overlap area changing accelerometer, all the damping mechanism can be assumed to come from Coutte-flow[5]. For this reason, the damping and mechanical thermal noise (or Brownian noise) of the overlap area changing accelerometer is lower than the gap changing one, as it can be seen from Table 3.2. These values are calculated by using MABEMS.

Table 3.2: Damping coefficients and spectral density of Brownian noise

	Gap Changing Design	**Overlap Area Changing Design**
Coutte-flow Damping Coefficient	0.7 10^{-6} Ns/m	1.6 10^{-6} Ns/m
Hagen-Poiseuille flow Damping Coefficient	1.72 10^{-6} Ns/m	7.05 10^{-11} Ns/m
Total Damping Coefficient	2.42 10^{-6} Ns/m	1.6 10^{-6} Ns/m
Spectral Densitiy of Brownian Noise	60 10^{-6} g/$\sqrt{\text{Hz}}$	31.46 10^{-6} g/$\sqrt{\text{Hz}}$

3.3.4 Nominal Capacitance Calculation and Fringing Field Analysis

Poisson's equation should be solved in 3-D to accurately calculate the capacitance of a given sytem:

$$\vec{\nabla} \bullet \vec{\nabla} V(x,y,z) = \nabla^2 V(x,y,z) = div(gradV) = -\frac{\rho}{\varepsilon} \tag{3.1}$$

where ρ is the space charge, V is the electrical potential, and ε is the dielectric constant. It is not always possible to obtain analytical results from equation (3.1). In general, this problem is solved numerically by using finite element methods [33].

Analytical models for calculating the capacitance can be divided in two:

---

[5] Coutte-flow damping is not only caused by the motion of air between the proof-mass and substrate, and it is also caused by the same mechanism between the fixed and movable fingers (there is sliding film between them) for overlap area changing design.

- Simplified formula for parallel plate capacitors. This model is only valid when the gap between the electrodes is small compared to the extent of the electrodes as fringing fields are neglected.
- Analytic formulations including fringing fields

In our design, the extent of the electrodes ($t_{poly}=2\ \mu m$) are comparable, actually equal ($g_0=2\ \mu m$) with the gap, parallel plate model is therefore expected to estimate a capacitance smaller than the results from FEA. The model including fringing fields can not be accounted for by one single formula. Several approximate models have been derived, a few of these are well studied in [34]. For instance, H.B Palmer derived the following expression for capacitance per unit lenght.

$$C = \varepsilon \frac{w}{g_0}\left[1 + \frac{g_0}{\pi w} + \frac{g_0}{\pi w}\ln\left(\frac{2\pi w}{g_0}\right)\right] \tag{3.2}$$

Figure 3.10 shows how the Palmer model, including fringing fields, converge towards the model not including fringing fields as the ratio between the width over gap increases. This model is however only valid for a two electrode configuration, but illustrates the effect of fringing fields on capacitance value.

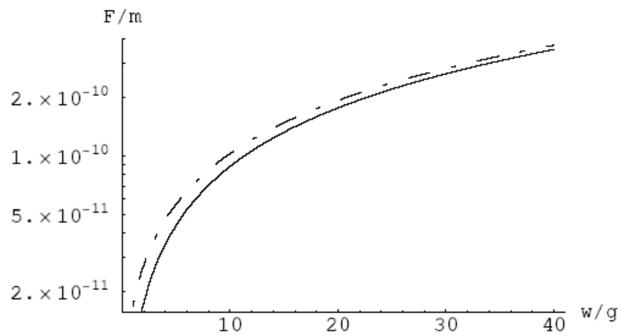

Figure 3.10: Convergence of Palmer's formula to parallel plate model for normalized dimensions

For the simplification purpose, the parallel plate capacitance model is used for the analysis of the system, along this work. Since the many previously realized designs [35,9,15,19,28], which use the similar processes to MUMPS, utilize the same approximation, the error coming from the fringing fields is ignored, in this work, too. And, also inclusion of the the fringing field effect to the analytic models is very difficult, even impossible without numerical methods. So, by utilizing the parallel plate model the nominal capacitance (C_0) is found $129.6x10^{-15}$ *Fahrad* for overlap area changing accelerometer and $115.6x10^{-15}$ *Fahrad* for gap changing accelerometer. Despite the parallel plate model is used in this work, a 2-D electrostatic finite element analysis is carried out to show the effect of the fringing fields. To find the distributed potential, five electrode configuration from gap changing accelerometer is used. Voltage on the movable finger (square at the middle of Figure 3.11) is set to *100 Volts* while all counter electrodes (fixed fingers and substrate) are grounded. The fringing fields from movable finger to substrate and outer fixed electrodes can be seen in Figure 3.11. As it is obvious from Figure 3.11, FEA results also confirm that the parallel plate capacitance model is a good approximation for our design since the most of the distributed potential occurs between the movable finger and adjacent fixed fingers.

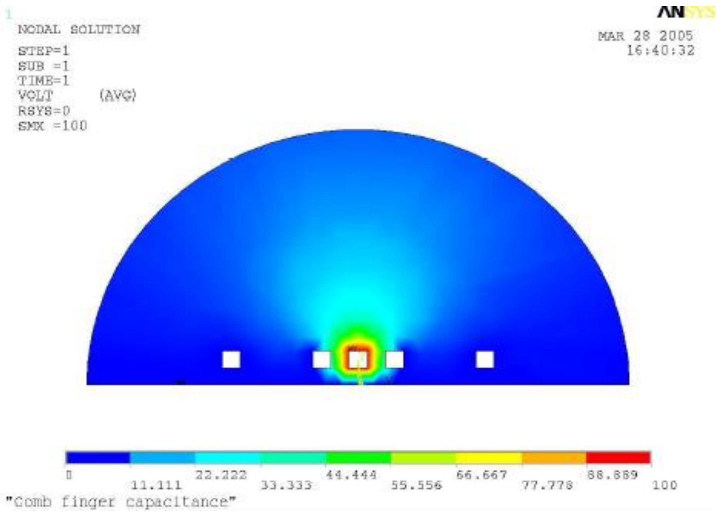

Figure 3.11: FEA result of distributed potential for five electrode configuration of gap changing accelerometer

3.3.5 Simulation Results and Frequency Response of Mechanical Devices

With the considerations described in Section 2, it is possible to derive a mathematical model for the micromachined sensing elements. Mathematical model of the accelerometer, represented with the blocks, is shown in Figure 3.12 [31]. This model includes the dynamic model of mechanical system, spring softening effect, and capacitive position sensing. The saturation block models the constraint in movement of the movable fingers by the fixed electrodes. Numerical value of this constraint is $\pm 2\ \mu m$ for gap changing design and $\pm 6\ \mu m$ for overlap area changing design. As it can be understood from the Figure 3.12, sensing element is itself behaves like a closed loop system in its own right since the damping force and spring force forms the negative feedback signals of the system.

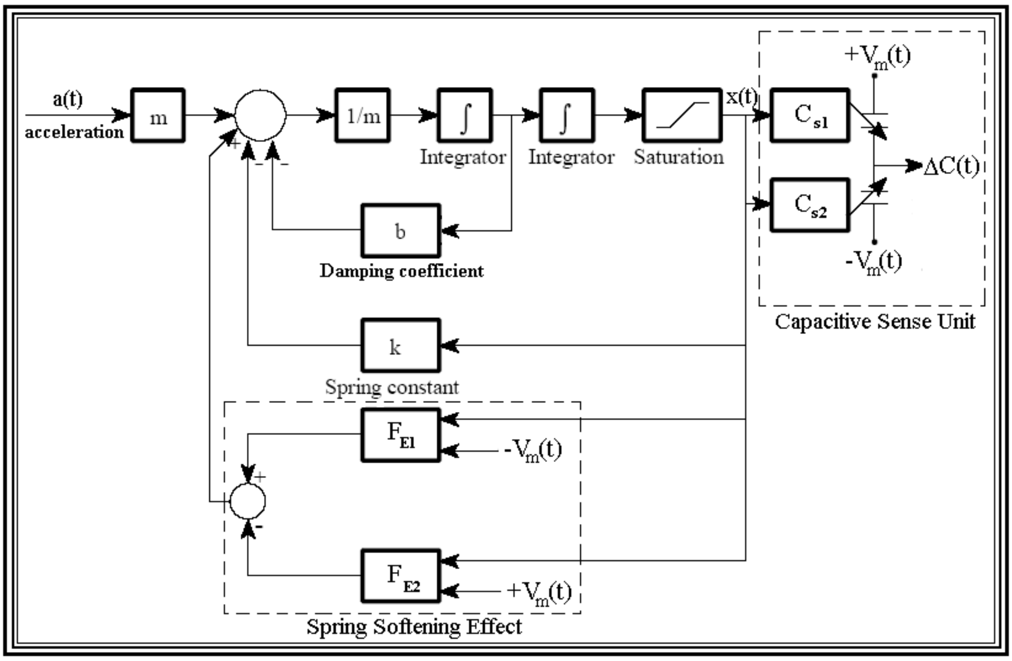

Figure 3.12: Mathematical model of MEMS accelerometer (Adapted from [31])

The mathematical model in Figure 3.12, is implemented in a standart simulation package, named SIMULINK, by using the obtained parameters along this section. In addition, the Brownian noise is superimposed to the input acceleration. Figure 3.13 shows the SIMULINK implementation of the gap changing (the upper blocks) and overlap area changing (the lower blocks) accelerometers. Since the frequency of the modulation signals ($V_m(t)$) should be much higher than the bandwidth of the accelerometers ($\approx f_r$), it is selected *1 MHz*. As it is stated in Section 2.5, spring softening effect is not valid for the overlap are changing design so this effect is not included into its SIMULINK implementation.

Figure 3.14 shows the step response of the accelerometers for *1g* input acceleration. The output signal is the capacitance change at the output of the sense unit. As it is expected, the response time of the gap changing design is shorter than the other because of the wider bandwidth. From the SIMULINK simulation results, the acceleration to capacitance sensitivity is found $6.42x10^{-16}$ *F/g* for the gap changing design and $3.0x10^{-17}$ *F/g* overlap area changing design. The sensitivity of the overlap area changing design is *21.4* times lower than the gap changing design as it is expected from the explanations in Section 2.3.

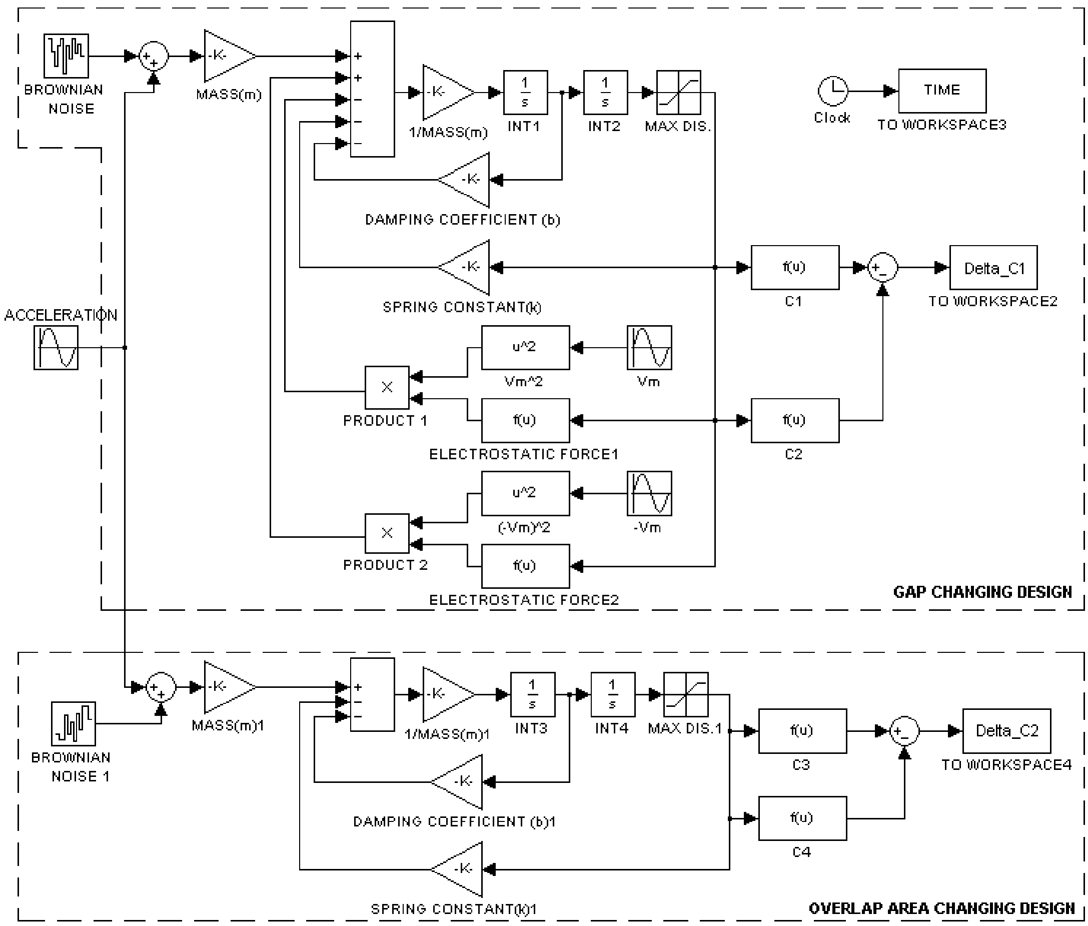

Figure 3.13: SIMULINK implementation of the MEMS accelerometers

Figure 3.15, drawned by using MABEMS, shows the frequency responses of the accelerometers. The horizantal axis represents the frequency while the vertical axis represents the amplitude of the displacement. Both axis is drawned in logarithmic scale. As it can be understood from the sharp peaks at resonant frequencies, both system is under damped. The quality factor is calculated *5.98* for gap changing design and *8.78* for overlap area changing design. In the phase response, for the values well below the resonant frequency, the phase angle is approximately 0^0 but for the frequencies higher than the resonant it becomes 180^0. For this reason, if the system is operated in closed-loop, phase compensation is needed to prevent the feedback to be positive.

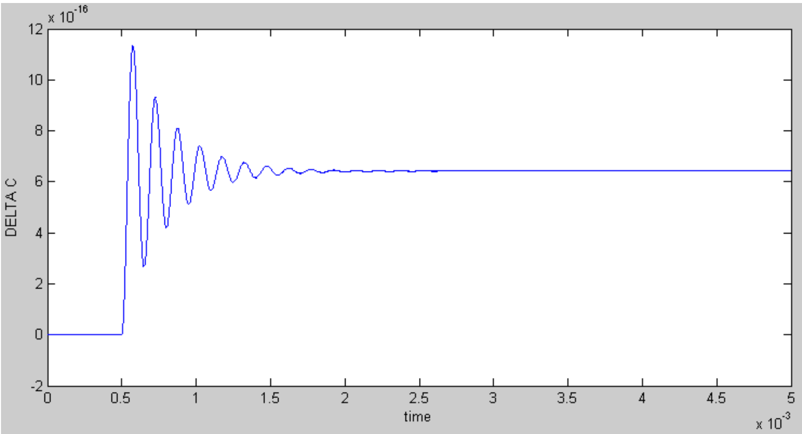

(a)

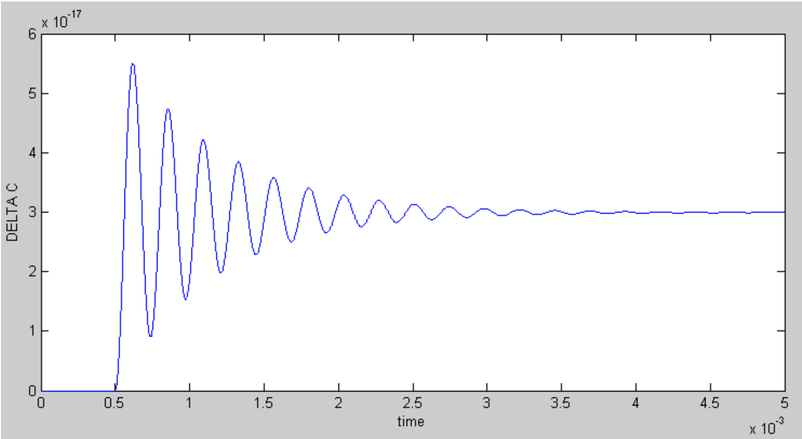

(b)

Figure 3.14: Step responses of (a) gap changing (b) overlap area changing accelerometers for 1g input acceleration

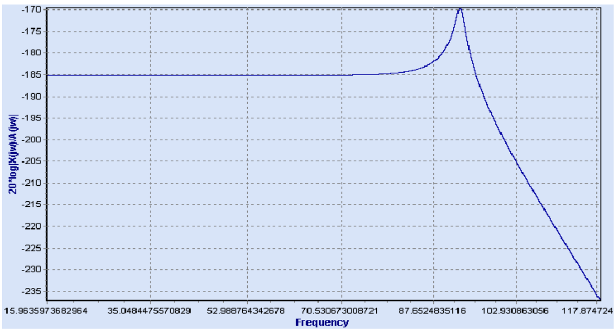

(a)

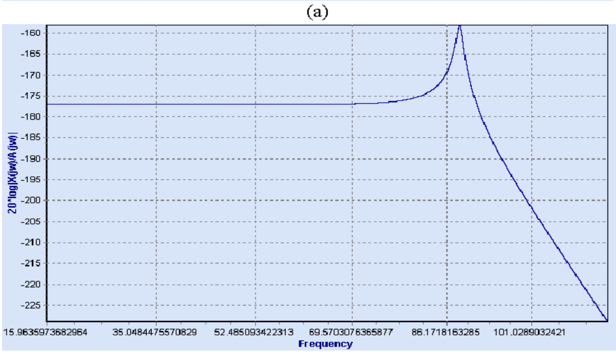

(b)

Figure 3.15: Mechanical Frequency Response (Amplitude) of (a) gap changing (b) overlap area changing accelerometers

3.4 Design of Electronic Circuit Interface

In this section, the electronic sensing interface is explained. For open-loop designs, this interface can be separated in two; signal pick-off circuit and demodulation circuit. At schematic level, circuit topology, similar to the topology described in [31], is utilized in this work.

3.4.1 Signal Pick-off Circuit

Full realization of the signal pick-off circuit is shown in Figure 3.16. The charge amplifier configuration is used, since it eliminates the effect of parasitic capacitances (Section 2.3). C_{s1} and C_{s2} represents the variable capacitors of the capacitive sense unit. Since the circuit functions like an integrator, d.c. signal that may be present at the proof-mass (the centre point between the variable capacitors) could cause the saturation at the output of operational amplifier (op-amp). For this reason, C_{dc} is placed between the proof-mass and op-amp to block any d.c. signal. Node between the variable capacitors can be at an undefined potential without R_{ref} . So, this resistor keeps the node between the variable capacitors at a defined potential and should be selected sufficiently large, such that the cut-off frequency of the highpass filter formed by R_{ref} and $C_{s1\ or\ s2}$ should be at least a hundred times lower than the frequency of the modulation signals (i.e., $f_{cut\text{-}off}=1/[2\pi\ R_{ref}\ C_{s1\ or\ s2}]< f_m/100=10\ KHz$). From this condition, the value of the R_{ref} is selected $200\ M\Omega$. R_f is used for obtaining the d.c. feedback for op-amp. The value of this resistor should be sufficiently high for minimizing the phase-shift of the voltage at the output of op-amp. To determine the unknown component values, the output voltage ($V_{out}(s)$) has to be defined. By using the current equalities and op-amp equation, we can write:

$$sC_{s1}[-V_m(s)-V_y(s)]+sC_{s2}[V_m(s)-V_y(s)]=\frac{V_y(s)}{R_{ref}}+sC_{dc}[V_y(s)-V_x(s)] \quad (3.3)$$

$$[V_x(s)-V_{out}(s)]\left(\frac{1}{R_f}+sC_f\right)=sC_{dc}[V_y(s)-V_x(s)] \quad (3.4)$$

$$-V_x(s)A_v=V_{out}(s) \quad (3.5)$$

From the equations (3.3), (3.4), and (3.5) $V_{out}(s)$ is obtained as:

$$V_{out}(s) = -\frac{sC_{dc}[-sC_{s1}V_m(s) + sC_{s2}V_m(s)]}{\left[\left(1+\frac{1}{A_v}\right)\left(\frac{1}{R_f}+sC_f\right)\left(s(C_{s1}+C_{s2}+C_{dc})+\frac{1}{R_{ref}}\right)+\frac{sC_{dc}}{A_v}\left(s(C_{s1}+C_{s2})+\frac{1}{R_{ref}}\right)\right]} \tag{3.6}$$

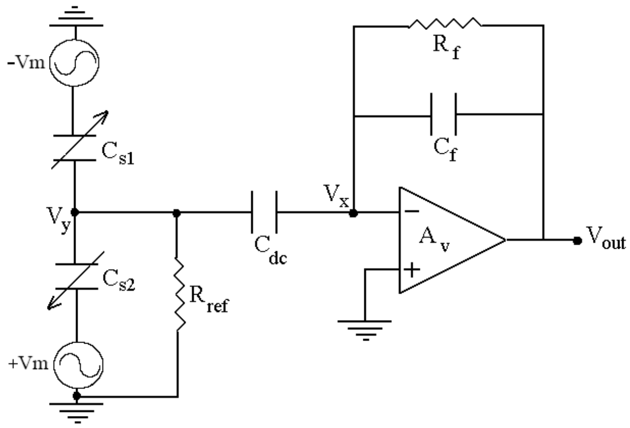

Figure 3.16: Signal pick-off circuit for sensing the capacitance change

If C_{dc} is selected *22 pF* then we can make the assumption that $C_{dc} >> (C_{s1}+C_{s2})$. Also, by using another assumption $1/R_{ref} \rightarrow 0$, equation (3.6) can be rewritten as:

$$V_{out}(s) = -\frac{R_f[-sC_{s1}V_m(s) + sC_{s2}V_m(s)]}{\left[\left(1+\frac{1}{A_v}\right)(1+sC_fR_f)+\frac{s(C_{s1}+C_{s2})R_f}{A_v}\right]} \tag{3.7}$$

C_f is selected *0.47 pF* and R_f is selected *1 MΩ*. The open-loop gain of the op-amp is assumed to be sufficiently high. Hence, we can make the assumptions that $|sC_fR_f| >> 1$, $C_f >> \left(\frac{C_{s1}+C_{s2}}{A_v}\right)$, and $\frac{1}{A_v} << 1$. Consequently, we arrive:

$$V_{out}(t) = -\frac{(C_{s2}-C_{s1})V_m(t)}{C_f} = -\frac{\Delta C}{C_f}V_m(t) \tag{3.8}$$

Equation (3.8) is obtained by assuming that the value of C_{s1} and C_{s2} capacitances are independent of time, but as it is explained in section 2.3, their values may change in time if a time dependent external acceleration effects to the proof-mass. An upper limit for the frequency of this time dependency is determined by the bandwith of the accelerometers and is not higher than 6847 Hz., (the resonant frequency of the gap changing accelerometer) for this work. So, since the frequency of the modulation signal *(1 MHz.)* is much higher than the bandwidth of the designed accelerometers, C_{s1} and C_{s2} is assumed to be quasi-stationary at above analysis. As it can be seen from equation (3.8), to have better performance even for low ΔC values (so acceleration) the output signal could be increased by selecting the C_f value as small as possible. But there is a lower limit for C_f defined by the settling time of the system. If it is decreased much, the settling time of the system increases. So, an optimum value is selected for C_f as we determined earlier as *0.47 pF*. R_{ref} and R_f can be implemented by using the MOS transistors that operates at subthreshold region or reverse biased diodes since they do not require precise values.

3.4.1.1 Operational Amplifier Design

In accelerometer system, there are two main noise source, one is the thermal noise (Brownian) of the mechanical system and the other is thermal noise from the electronic interface. Total noise determines the minimum detectable acceleration of the system. Especially, in low-g applications noise level should be made as low as possible. The minimum detectable acceleration determined by the total input acceleration noise:

$$a_{\min} = \sqrt{a^2_{electronic circuit} + a^2_{Brownian}} \tag{3.9}$$

As it can be seen from the equation (2.37), Brownian noise can be made low by optimizing the mass and damping factor of the system. In low-g applications vacuum packaging of the system is preferred to decrease the damping factor. For electronic interface main contributer of the noise comes from the components in signal pick-off circuit. For this reason, the design of this stage (especially operational amplifier) is very important since it operates with very low amplitude signals. And also, as it is understood from the analysis of the pick-off circuit in section 3.4.1, the gain and the input impedance of the operational amplifier should be very high. Schematic of designed CMOS operational amplifier is shown in Figure 3.17 [36]. This is a two stage operational amplifier. At the input stage PMOS transistors are used since their noise performance better than the NMOS transistors. M4 is the active load of the current mirror formed by M7 and M8 so, it forms the reference current. Also, M9 behaves like the active load of the second stage.

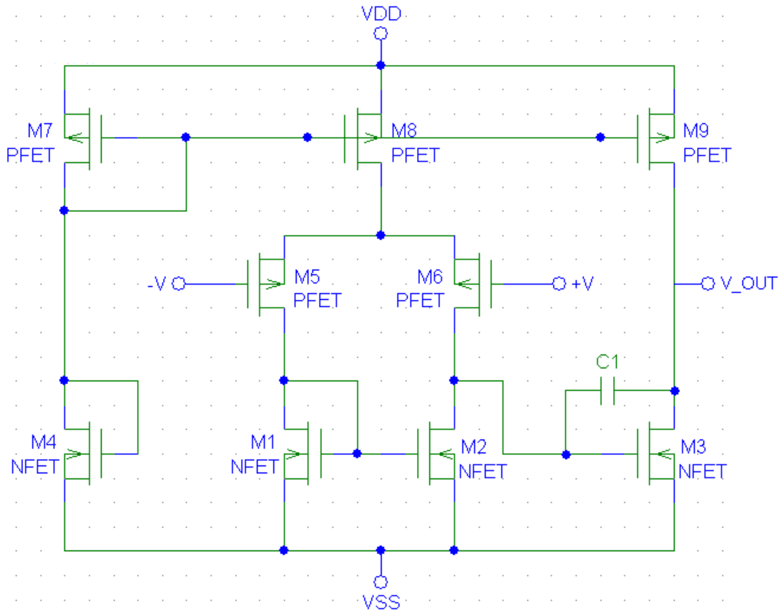

Figure 3.17: Schematic of the designed operational amplifier (Adapted from [36])

All the transistors can be modelled as an ideal MOSFET and a voltage noise source at the gate input. By using this model for all transistors in Figure 3.17, the spectral density of the input referred voltage noise for operational amplifier is [36]:

$$\overline{v^2_{op-amp\ in}} = \overline{v^2_{n5}} + \overline{v^2_{n6}} + \left(\frac{g_{m2}}{g_{m5}}\right)\left(\overline{v^2_{n1}} + \overline{v^2_{2}}\right) + \frac{\left(\overline{v^2_{n3}} + \left(\frac{g_{m9}}{g_{m3}}\right)\overline{v^2_{n9}}\right)}{K_d^2} \tag{3.10}$$

where $\overline{v^2_{nk}}$ is the spectral density of the voltage noise of k^{th} tranzistor, g_{mk} transconductance of k^{th} tranzistor, and K_d is the gain of the first stage (differential amplifier). For the frequencies that satisfy the $K_d >> 1$ condition (this is the case for our design), the last term at the right hand side of the equation (3.10) can be easily ignored. As it can be seen from the second term in equation (3.10), to eliminate the noise contribution of M1and M2 transistors, $g_{m5} >> g_{m2}$ condition should be satisfied. Under these conditions, total noise is formed by the input tranzistors (i.e., M5 and M6). Flicker noise (*1/f* noise) of these transistors can be ignored for our design since the frequency of the modulation signal is sufficiently high (*1 MHz*). In our design, thermal (Johnson) noise of the MOSFET is dominant. Thermal noise model of MOSFET is defined as in equation (3.11).

$$\overline{v_n^2} = \frac{8k_B T}{3}\frac{1}{g_m}\Delta f = \frac{8k_B T}{3}\frac{1}{\sqrt{2\mu C_{ox}\left(\frac{W}{L}\right)I_d}}\Delta f \tag{3.11}$$

where k_B is Boltzmann constant, T is temperature, μ is carrier mobility, C_{ox} is gate capacitance per area, W is the width of channel region, L is the lenght of channel, and I_d is the current flowing through the drain. From the equation (3.11), it is obvious that the width to lenght ratio of the input transistors should be as high as possible to decrease the input referred equivalent noise of the operational amplifier. Also, this condition is necessary for obtaining the high gain value. At the design phase of the op-amp one more point to consider is systematic imbalance. To prevent this situation, below condition should be satisfied:

$$\frac{(W/L)_1}{(W/L)_3} = \frac{(W/L)_2}{(W/L)_3} = \frac{(W/L)_9}{2(W/L)_8} \tag{3.12}$$

By taking above conditions into consideration, *(W/L)* ratio of the input transistors is selected *(100/1)*. The reference current for current mirror is made *31.1* μA by adjusting the *(W/L)* ratio of M4. Supply voltages are *2.5 V* and *–2.5 V*. The result of PSPICE simulation (without C1) shows *99.3 dB* of open loop gain and *95.6* μV offset voltage. The first pole of designed op-amp is at *418 KHz* (cut-off frequency) where the *3 dB* decrease occurs in frequency characteristic and second pole is at *100 MHz*. AC and DC characteristics (without C1) of the designed operational amplifier is shown in Figure 3.18. Since, in our design, the operational amplifier is operated by applying negative feedback (Figure 3.16), a compensation capacitance (C1) should be connected between the input and output of the second gain stage for assuring the stability of the charge amplifier system.

3.4.1.2 PSPICE Implementation of Mechanical Devices and Pick-off Circuit

PSPICE is a commercial software package that allows the simulation of the electronic circuits. Also, it is also possible to simulate the general engineering systems in this environment. We combined the mechanical device and pick-off circuit in this environment by using the mathematical model, given in section 3.3.5, of the accelerometer system. This mathematical model is implemented by using the components in Analog Behavioral Modelling Library (ABM) which is available in

PSPICE. PSIPCE Implemention of mechanical device and pick-off circuit for gap changing design is shown in Figure 3.19. YX variable admitance subcircuit, in Figure 3.19, is used to model the variable sense capacitance of accelerometers [31].

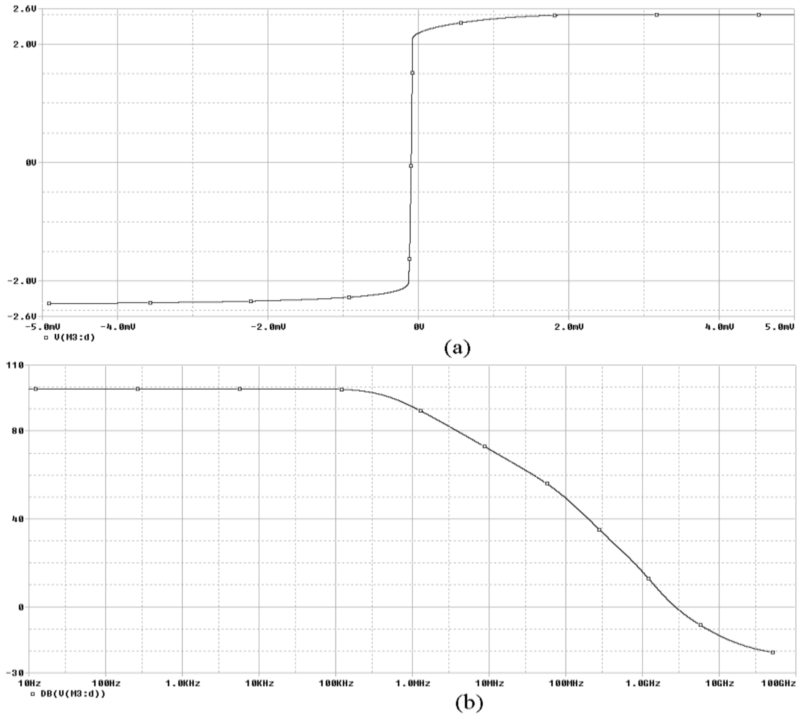

Figure 3.18: (a) DC characteristic and (b) AC (amplitude) characteristic of designed operational amplifier

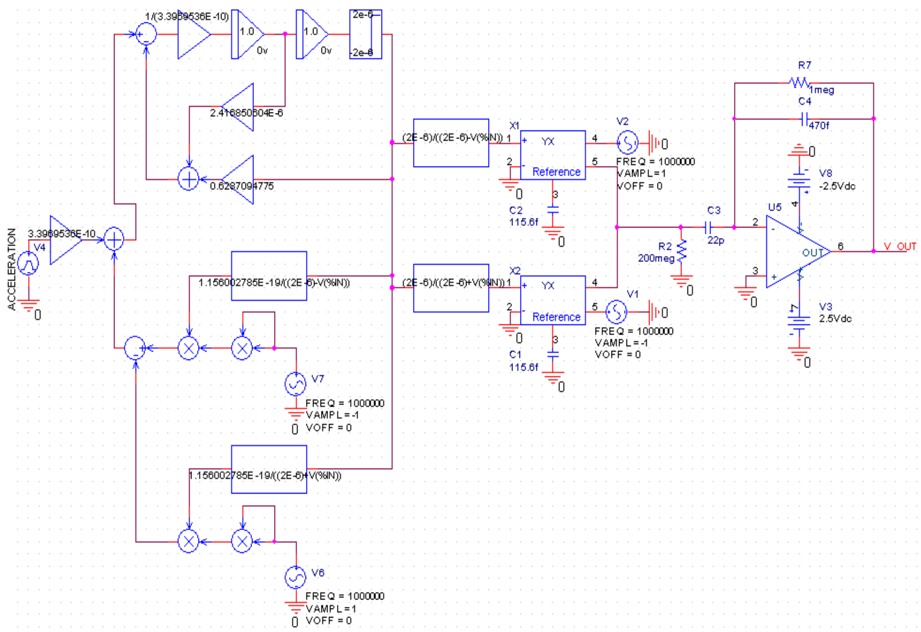

Figure 3.19: PSPICE implementation of mechanical device and pick-off circuit of gap changing accelerometer

PSPICE simulation result of both system is given in Figure 3.20. In this figure the output voltage of the pick-off circuit for the input acceleration of *10 g* is shown. As it is expected, the output of the signal pick-off circuit is an amplitude modulated signal with *1MHz* (frequency of the modulation signals) carrier frequency. So, this signal should be demodulated to obtain meaningful output. The ratio of the acceleration to capacitance sensitivity of the gap changing design and overlap area changing design was obtained *21.4* in Section 3.3.5. Since the amplitude of the modulation signal is selected *1 V* for gap changing and *2 V* for overlap area changing design, it is expected that the ratio of the voltage to acceleration sensitivities must be *10.7* according to the equation (2.8) or (3.8). Really, from the results in Figure 3.20, it can be seen that the ratio of the sensitivities is nearly same as the expected value of *10.7*.

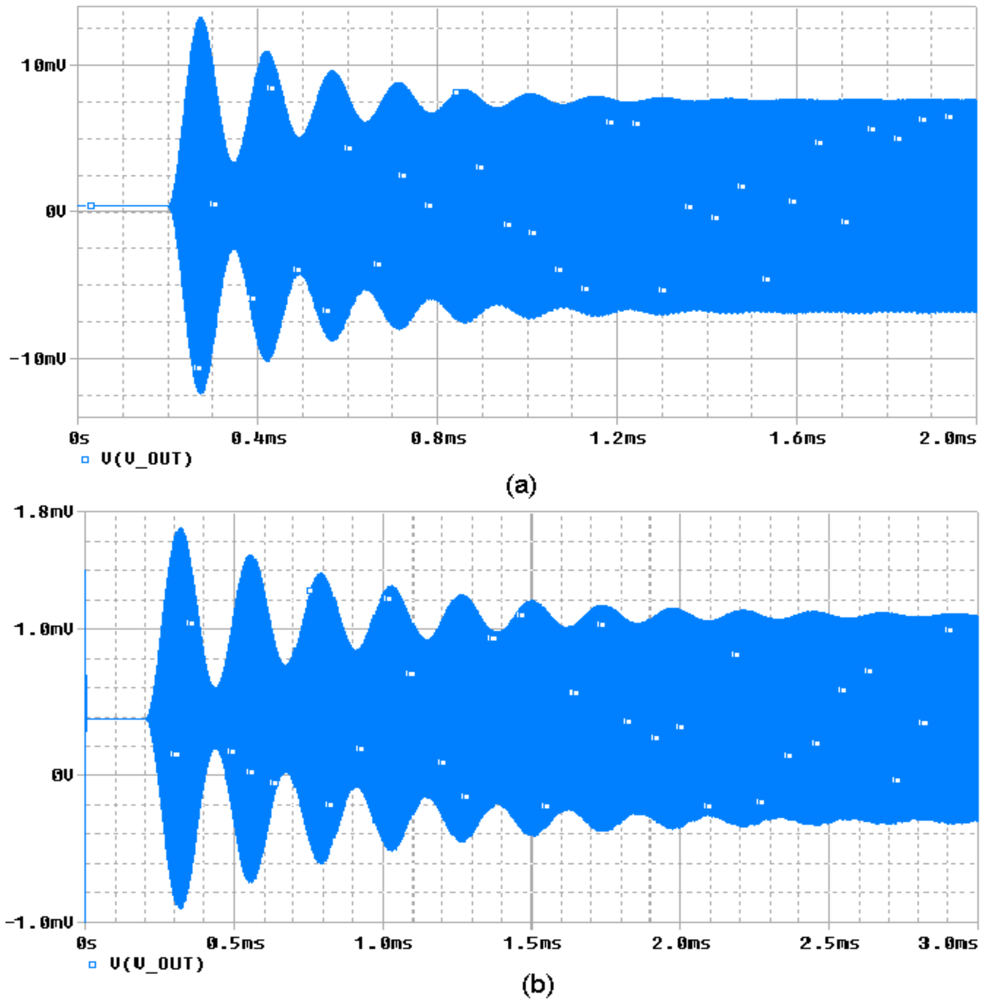

Figure 3.20: Output voltage of the pick-off circuit (input is 10g step acceleration) of (a) gap changing (b) overlap area changing design

4 CONCLUSION AND FUTURE WORK

The main goal of this work is to explain the operation, theory and the analysis of the capacitive surface micromachined accelerometer and complete the design of the micro-accelerometer system that has the capability of measuring in high dynamic range. In conventional methods, accelerometers are operated in closed loop by applying feedback signals to increase the dynamic range. In this work, a new method is offered and described conceptually as an alternative to the conventional closed loop systems and this method is named as Force Feed Forward Mechanism. In this method, less sensitive system, forms the dynamic offset of the more sensitive device. For this purpose, two separate mechanical devices are designed. One of these systems utilizes the changing gap between the comb fingers to sense the capacitance change. This sytem has high sensitivity but nonlinearty occurs after a certain displacement. In this work, the sensitivity of this system is found $6.42x10^{-16}$ *F/g*. The other system utilizes the changing overlap area between the comb fingers to sense the capacitance change. As it is proved in section 2, this sytem has lower sensitivity than the other one but linear even for large displacements. And the sensitivity of this system is found $3.0x10^{-17}$ *F/g* for our design. These accelerometers are designed by using PolyMUMPs surface micromachining process and the total area of the design is *1552 μm x 851 μm*. Effective area, including fixed fingers and springs, of gap changing accelerometer is *541 μm x 652 μm* and, overlap area changing accelerometer is *898 μm x 424 μm*. To realize such a system the direction of the comb fingers of two device is made perpendicular to each other while the devices are located on the substrate. For the optimization of the mechanical system at behavioral level, by using the analytical models obtained in Section 2, visual software, named MABEMS, is implemented in C++ programming language. Results that are found by this software are in good agreement with the FEA simulation results. Mathematical model of the accelerometer, obtained in Section 3, is implemented in PSPICE by using the Analog Behavioral Modelling (ABM) library so, this allowed the simulation of the mechanical device and electronic interface in the same environment. For using in signal pick-off circuit a low noise and high gain op-amp is designed.

The future work includes the design of demodulation circuit and the design of the compensator and force feedforward unit. The detailed analysis and the analytical model of the force feedforward sytem should be determined. So the advantages and the disadvantages of the force feedforward mechanism is better determined. The overall electronic circuit interface may be implemented on single die by using appropriate technology (Application Specific IC -ASIC) for obtaining better performance.

REFERENCES

[1] **Kovacs, Gregory T.A.,** 1998. Micromachined Transducers Sourcebook, The McGraw-Hill Companies, Inc.

[2] **Senturia, S.D.,** 2000. Microsystem Design, Kluwer Academic Publishers.

[3] **Heck, J.M.,** 2001. Pollycrystalline Silicon Germanium for Fabrication, Release, and Packaging of Microelectromechanical Systems, University of California at Berkley, *Ph. D. dissertation.*

[4] **Maluf, N,.** 2000. Introduction to Microelectromechanical System Engineering, Artech House, Inc.

[5] **Cheng, Z., Huang, W., Cai, X., Xu, B., Luo, L. and Li, X.,** 2002. A Study of Packaging Effects on the Performances of MEMS for High-G Accelerometers, *IEEE Int'l Syposium on Electronic Materials and Packaging*, pp. 231-238

[6] **Stark, B.,** 1999. MEMS Reliability Assurance Guidelines for Space Applications, NASA, JPL Publication 99-1, California.

[7] **Sharpe, W.N, Yuan, F.B., Vaidyanathan, R. and Edwards, R.L.,** 1997. Measurements of Young's Modulus, Poisson's Ratio, and Tensile Strenght of Polysilicon, *Proceedings of the Tenth IEEE International Workshop on Microelectromechanical Systems*, Nagoya, Japan, pp.424-429

[8] **MultiMEMS Microsystems Manufacturing Cluster.,** 2003. MultiMEMS Process, Design Handbook, Version 3.0, Part IIIa:Design Introduction, MultiMEMS.

[9] **Analog Devices.,** 2002. ADXL210E Low cost +-10g Dual Axis Accelerometer with Duty Cycle, Data Sheet, Rev.0, Analog Devices, Inc.

[10] **Motorola.,** 2003. Sensor Device Data Book, DL/200D, Rev. 5, Motorola, Inc.

[11] **Acar, C. and Shkel, A.,** 2003. Experimental Evaluation and Comparative Analysis of Commercial Variable-Capacitance MEMS Accelerometers, *Journal of Micromechanics and Microengineering*, **13**, 634-645

[12] **STM.,** 2004. LIS2L02AQ Inertial Sensor:2 Axis 2g/6g Linear Accelerometer, Data Sheet, Rev. 3, STM, Inc.

[13] **Boser, B.E. and Howe, R.T.,** 1996. Surface Micromachined Accelerometers, *IEEE Journal of Solid-State Circuits*, Vol. 31, no.3, pp. 366-375

[14] **Chae, J., Kulah, H., Salian, A. and Najafi, K.,** 2000. A High Sensitivity Silicon-On-Glass Lateral μg Microaccelerometer, *Third Annual Micro/Nano Technology Conference*, Houston, Texas.

[15] **Baschirotto, A., Gola, A., Chiesa, E., Lasalandra, E., Pasolini, F., Tronconi, M. and Ungaretti, T.,** 2003. A +-1-g Dual-Axis Linear Accelerometer in a Standart 0.5 μm CMOS Technology for High-Sensitivity Applications, *IEEE Journal of Solid-State Circuits*, Vol. 38, no.7, pp. 1292-1297

[16] **Takao, H., Fukumoto, H.and Ishida, M.,** 2001. A CMOS Integrated Three-Axis Accelerometer Fabricated with Commercial Submicrometer CMOS Technology and Bulk-Micromachining, *IEEE Transactions on Electron Devices*, Vol. 48, no.9, pp. 1961-1968

[17] **Luo, H., Fedder, G.K. and Carley, R.,** 2000. A 1 mg Lateral CMOS-MEMS Accelerometer, *in Proceedings of the 13th IEEE International Conference on Micro Electro Mechanical Systems (MEMS '00)*, pp. 502-507, Miyazaki, Japan.

[18] **Lemkin, M. and Boser, E.B.,** 1999. A Three-Axis Micromachined Accelerometer with a CMOS Position-Sense Interface and Digital Offset-Trim Electronics, *IEEE Journal of Solid-State Circuits*, Vol. 34, no.4, pp. 456-468

[19] **Lemkin, M., Boser, E.B., Auslander, D. and Smith, J.M.,** 1997. 3-Axis Force Balanced Accelerometer Using a Single Proof-Mass, *IEEE International Conference on Solid-State Sensors and Actuators*, Chicago. pp.1185-1188

[20] **van Drieenhuizen, B.P., Maluf, N.I., Opris, I.E. and Kovacs, G.T.A.,** 1997 Force-Balanced Accelerometer with mG Resolution, Fabricated Using Silicon Fusion Bonding and Deep Reactive Ion Etching, *IEEE International Conference on Solid-State Sensors and Actuators*, Chicago. pp.1229-1230

[21] **Seshia, A.A., Palaniapan, M., Roessig, T.A., Howe, R.T., Gooch R.W., Schimert T.R. and Montague, S.,** 2002. A Vacuum Packaged Surface Micromachined Resonant Accelerometer, *IEEE Journal of Microelectromechanical Systems*, Vol. 11, no.6, pp. 784-793

[22] **Dauderstadt, U.A. and French, P.J.,** 1998. A Thermal Accelerometer, *Proc. of SAFE98*, Mierlo.

[23] **Koester, D., Cowen, A., Mahadevan, R., Stonefield, M. and Hardy, B.,** 2003. PoyMUMPS Design Handbook, Revision 10.0, MEMSCAP

[24] **Boser, B.E.,** 1997. Electronics for micromachined inertial sensors, *Transducers Dig. Of Tech. Papers*, pp.1169-1172

[25] **Boser, B.E. and Howe, R.T.,** 1995. Surface Micromachined Accelerometers, *IEEE Custom integrated Circuits Conference*, pp. 337-344

[26] **Weigold, J.W., Najafi K. and Pang, S.W.,** 2001. Design and Fabrication of Submicrometer, Single Crystal Si Accelerometer, *IEEE Journal of Microelectromechanical Systems*, Vol. 10, no.4, pp. 518-524

[27] **Starr, J.B.,** 1990. Squeeze-film Damping in Solid State Accelerometer, *IEEE Solid-State Sensor and Actuator Workshop*, pp. 44-47, Hilton Head Island.

[28] **Zhou, Y.,** 1998. Layout Synthesis of Accelerometers, Carnegie Mellon Universty, *M.S. Thesis*

[29] **Fedder, G.K.,** 1994. Simulation of Microelectomechanical Systems, Universty of California at Berkley, *Ph. D. Thesis*

[30] **Kuehnel, W.,** 1995. Modelling of the Mechanical Behaviour of a Differential Capacitor Acceleration Sensor, *Sensors and Actuators*, A, no.48, pp. 101-108

[31] **Kraft, M.,** 1997. Closed Loop Digital Accelerometer Employing Oversampling Conversion, Coventry Universty, UK, *Ph. D. dissertation*.

[32] **Kajita, T., Moon, U.K. and Temes G.C.,** 2001. A Noise Shaping Accelerometer Interface Circuit for Two-Chip Implementation, *IEEE Instrumentation and Measurement Technology Conference* pp. 1581-1586, Budapest, Hungary.

[33] **Barke, E.,** 1988. Line-to-Ground Capacitance Calculation for VLSI: A Comparison, *IEEE Transactions on Computer-Aided Design*, Vol. 7, no. 2, pp 295-298

[34] **Leus, V. and Elata, D.,** 2004. Fringing Field Effect in Electrostatic Actuators, Technion-Israel Institute of Technology, Faculty of Mechanical Engineering, *Technical Report ETR-2004-2*

[35] **Boser, B.E.,** 1997. Capacitive Interfaces for Monolithic Integrated Sensors, Chapter in "RF Analog-to-Digital Converters; Sensor and Actuator Interfaces; Low-Noise Oscillators, PLLs and Synthesizers," R.J. van de Plassche, J. H. Huijsing, and W. M. C. Sansen (eds.), Kluwer Academic Publishers.

[36] **Kuntman, H.K.,** 1997. Analog MOS Tümdevre Tekniği, İstanbul Teknik Üniversitesi Rektörlüğü, İstanbul.

APPENDIX A

```
C=[165.6, 63.98, 63.98,0,0,0;       %Stiffness Matrix Coefficients
  63.98, 165.6, 63.98,0,0,0;
  63.98, 63.98, 165.6,0,0,0;
  0,0,0, 79.51,0,0;
  0,0,0,0, 79.51,0;
  0,0,0,0,0, 79.51];
S=inv(C);                           %Inverse of Stiffness Matrix
S11=S(1,1);
S12=S(1,2);
S44=S(4,4);
teta=0:0.001:2*pi;                  %Direction cosines
l1=cos(teta);
l2=cos(pi/2-teta);
l3=0;
A=(S11-2*(S11-S12-0.5*S44)*(l1.^2.*l2.^2+l2.^2.*l3.^2+l3.^2.*l1.^2));
E=1./A;                             %Apply Brantley's Formula
polar(teta,E,'-b');                 %Plot in the polar coordinates
grid on
title('Youngs Modulus (GPa)')
xlabel(strcat('Max=',num2str(max(E)),'GPa, Min=',num2str(min(E)),'GPa'))
text(max(E)*1.4,0,('[100]'));
text(-max(E)*1.6,0,('[100]'));
text(max(E)*1,max(E),('[110]'));
text(-max(E)*1.2,max(E),('[110]'));
text(-max(E)*1.2,-max(E),('[110]'));
text(max(E)*1,-max(E),('[110]'));
text(0,max(E)*1.4,('[010]'));
text(0,-max(E)*1.4,('[010]'));
```

Listing of the MATLAB programme to calculate the variation of Young’s Modulus with the crystal orientation for Single Crystal Silicon (SCS)

BIOGRAPHY

Özgür Erdener was born in Kırklareli, TURKEY in 1977. He graduated from Çanakkale Anotolian High School in 1995. He received B.Sc. degree in Electronics and Communication Engineering from Istanbul Technical University, in year 2000. Between the years 2000 and 2001, he worked as researcher at TUBITAK Semiconductor Technology Research Laboratory (YİTAL) in Gebze, İzmit. Between the years 2002 and 2004, he worked as a design engineer of industrial electronics at ENTES A.Ş, Istanbul. In 2002, he started to pursue M.Sc. degree in Electronics Engineering programme in the same university where he received B.Sc. degree. He has been still working as a design engineer of data communication systems at R&D department of ADAM Group of Companies, Istanbul.